

Physical characterisation of southern massive star-forming regions using Parkes NH_3 observations

T. Hill^{1*}, S. N. Longmore², C. Pinte¹, M. R. Cunningham³, M. G. Burton³
and V. Minier^{4,5}

¹ School of Physics, University of Exeter, Stocker Road, EX4 4QL, Exeter, UK

² Harvard-Smithsonian Center for Astrophysics, 60 Garden Street, Cambridge, MA 02138, USA

³ School of Physics, University of New South Wales, Sydney, 2052, NSW, Australia.

⁴ CEA, DSM, IRFU, Service d'Astrophysique, 91191 Gif-sur-Yvette, France

⁵ Laboratoire AIM, CEA/DSM - CNRS - Université Paris Diderot, IRFU/Service d'Astrophysique, CEA-Saclay, 91191 Gif-sur-Yvette, France

Accepted/Received

ABSTRACT

We have undertaken a Parkes ammonia spectral line study, in the lowest two inversion transitions, of southern massive star formation regions, including young massive candidate protostars, with the aim of characterising the earliest stages of massive star formation. 138 sources from the submillimetre continuum emission studies of Hill *et al.* were found to have robust (1,1) detections, including two sources with two velocity components, and 102 in the (2,2) transition.

We determine the ammonia line properties of the sources: linewidth, flux density, kinetic temperature, NH_3 column density and opacity, and revisit our SED modelling procedure to derive the mass for 52 of the sources. By combining the continuum emission information with ammonia observations we substantially constrain the physical properties of the high-mass clumps. There is clear complementarity between ammonia and continuum observations for derivations of physical parameters.

The MM-only class, identified in the continuum studies of Hill *et al.*, display smaller sizes, mass and velocity dispersion and/or turbulence than star-forming clumps, suggesting a quiescent prestellar stage and/or the formation of less massive stars.

Key words: line: profiles – stars: formation – stars: fundamental parameters – stars: early-type – ISM: molecules – masers.

1 INTRODUCTION

Massive stars are dynamical and enigmatic powerhouses that shape and drive both their local stellar neighbourhood and the ecology and evolution of their host galaxy. Despite this heavy influence, the formation and evolution of a massive star is not well understood. Particularly perplexing are the earliest evolutionary stages of massive star formation (MSF). The difficulty lies in the unambiguous detection, identification and characterisation of these stages, snapshots of which are difficult to obtain as a result of the general rarity of candidates and the rapidity of their evolution (Garay & Lizano 1999).

Whether or not massive stars are scaled-up analogs of low-mass stars is still uncertain. Massive stars exert

considerable radiative pressure on the surrounding dust and gas, which in principle could halt and reverse spherical infall of the collapsing protostar. Therefore, a ‘simple’ scaled-up version of low mass star formation is insufficient for massive stars. There are a number of different approaches to address this dilemma as outlined in the reviews by Evans *et al.* (2002); Menten *et al.* (2005); Zinnecker & Yorke (2007); Beuther *et al.* (2007).

As their sophistication increases numerical simulations in two and three dimensions show that the radiation pressure problems associated with spherical symmetry can be overcome (e.g. Krumholz *et al.* 2009). It is still not clear however, whether the bulk of the mass that finally ends up on the massive star comes from the monolithic collapse of a single dense core (e.g. McKee & Tan 2003) or is accreted from surrounding lower density gas which is funneled to the

* E-mail: thill@astro.ex.ac.uk

centre of a cluster's gravitational potential where the most massive stars are forming (e.g. Bonnell et al. 1998).

The natal molecular cloud, from which high-mass stars are formed, is expected to be dense, massive and cold, detectable only at (sub)millimetre wavelengths. Within the molecular cloud, core collapse will be triggered. As the collapsing protostar gains mass, the gravitational energy will serve to heat the core and ionise the surrounding material, causing an increase in the luminosity of the core. In terms of parameter evolution, the initial protostar will be massive, cool and of low luminosity. As the core evolves, it will accumulate more mass, and the temperature and luminosity of the core will increase. This evolution is seen in low mass protostars (Evans et al. 2002).

In a search for cold cores that would mark the earliest stages of massive star formation Hill et al. (2005) undertook a (1.2) millimetre SIMBA¹ continuum emission study of sources exhibiting signs of methanol maser and/or radio continuum emission - both of which have previously proven successful tracers of the earliest stages of massive star formation (e.g. Minier et al. 2000; Williams et al. 2004; Pestalozzi et al. 2005). This SIMBA survey revealed a large number of millimetre continuum sources (255) devoid of the maser and UC H₁₁ sources targeted. Subsequent submillimetre observations of these sources, which were dubbed 'MM-only cores', unveiled submillimetre equivalents for each - often revealing the multiplicity of individual MM-only sources, and confirmed their association with cold, deeply embedded objects (Hill et al. 2006).

The aforementioned SIMBA survey detected a total of 405 millimetre continuum sources, which (based on their star formation association) could be broken into four classes of source. Hill et al. (2005) proposed that each of these classes of source could represent a different phase of massive star evolution, with the MM-only class a possible example of the very earliest stages of massive star formation. A caveat however, is whether the MM-only cores are currently undergoing or will/can support massive star formation.

In order to determine the characteristic properties of the sources in the SIMBA sample, in particular the previously unknown and unstudied MM-only cores, Hill et al. (2009) performed spectral energy distribution (SED) modelling of a significant fraction of the sample. SED diagrams are useful tools from which physical quantities such as the luminosity, mass and temperature can be derived (cf. Whitney et al. 2003; Robitaille et al. 2006; Hill et al. 2009). If the observational data are well constrained (cf. Minier et al. 2005), SED modelling can provide useful estimates of each of these parameters, for each star-forming core, which allows estimation of the evolutionary phase of a young massive star.

The luminosity, mass and temperature of an astronomical source are fundamental physical attributes that may be used to clarify and characterise the nature of a source, possibly providing insight into their evolutionary status similarly as they do for low mass stars (André et al. 2000). Indeed, the temperature of a source places important physical constraints on the chemical composition of the core, including

which chemical species are present in the core, as well as the size and types of grains present in the central star-forming cores.

The method employed for the SED fitting was that of Bayesian inference, which enabled a statistically probable range of suitable values for the luminosity, mass and temperature, for each source modelled. As SED modelling is heavily reliant upon robust data, it was not possible to usefully constrain each of these parameters for a thorough assessment of massive star formation scenarios. In the absence of reliable far-infrared data, which would serve to constrain the peak of the SED and thus parameters resultant from the fit, additional means of constraining the source parameters, such as temperature, are necessary.

Ammonia is an excellent molecular cloud thermometer (Menten et al. 2005) from which the rotational temperature and ultimately the kinetic temperature of the source can be determined. Ammonia is readily detectable in quiescent dark clouds and regions of low luminosity (Ho & Townes 1983) making it perfectly suited to study the birthplace of massive stars. The ratio of the hyperfine components of ammonia's signature five-fingered spectrum provides the optical depth information of the molecular cloud environment. As NH₃ is a particularly good probe of high density gas, and is more resilient to the effects of depletion than other high density tracers (e.g. CS), ammonia observations also provide information pertaining to the density of the core (cf. Longmore et al. 2007, and references therein).

We have undertaken an ammonia spectral line survey of sources from the SIMBA sample of Hill et al. (2005) in order to obtain an independent determination of their temperature and simultaneously examine the robustness of our SED fitting (Hill et al. 2009). In addition to facilitating and constraining further SED fitting, these ammonia observations provide information pertaining to the molecular abundance of ammonia in the cores, as well as the physical parameters such as linewidth, rest velocity, column density and virial mass. With this information, we seek to address formation scenarios for massive stars and identify the star formation status/phase of the MM-only core.

2 OBSERVATIONS

We have undertaken a multi-inversion transition study of ammonia, in the lowest two inversion transitions, toward the SIMBA sample of Hill et al. (2005), with the aim of determining characteristic source properties, such as temperature and column density. The sample comprises four classes of millimetre continuum sources as alluded to in section 1: class M are sources with a methanol maser association, class R have radio continuum associations, class MR have both a maser and radio continuum source, whilst class MM are detected solely from their millimetre continuum emission.

The ammonia observations were undertaken on the Australia Telescope National Facility (ATNF) operated Parkes² radio telescope, using the new K-band receiver which operates from 16–26 GHz, during three nights spanning 2008,

¹ The SEST IMaging Bolometer Array (SIMBA) was a 37 channel hexagonal array on the Swedish ESO Submillimetre Telescope (SEST).

² <http://www.parkes.atnf.csiro.au/>

September 17–19. During this period, 244 sources were observed simultaneously in both NH_3 (1,1) and (2,2).

The K-band receiver, which was partially commissioned in September 2008, was used in conjunction with the digital filterbank-3 (DFB) backend which contains dual digitisers and Compact Array Broadband Backend (CABB)³ processors⁴. Although the Parkes telescope is 64 m in diameter, only the inner 55 m is used for observations at 23 GHz.

The NH_3 (1,1) and (2,2) observations were undertaken in position switch mode, using a bandwidth of 128 MHz centred at 23708 MHz to enable simultaneous observations of the two transitions. Maser velocities (Pestalozzi et al. 2005) were adopted as the rest velocity for each of the sources targeted. For those sources devoid of maser associations i.e. class R and MM, the velocity of the nearest coincident methanol maser was adopted as the rest velocity. We used 8192 channels to produce an expected velocity resolution of 0.2 km/s.

The pointing accuracy of the Parkes telescope is typically 10–15 arcsec which is smaller than the beamsize of 58 arcsec. The T_{sys} ranged from 85 to 132 K during the period of the observations (12–15 hr observing shifts), with a median of 96 K.

Typical integration times were 5 minutes per source. The rms noise in the spectra ranges from 0.13 to 0.30 Jy/beam for the NH_3 (1,1) transition and 0.13 to 0.25 Jy/beam for the (2,2) transition with the exception of one source (G 294.989-1.720) which had an rms of 0.86 and 0.87 Jy/beam for each of the transitions, respectively. The full set of spectra, including the sample spectra given in Figure 1, are presented in the Appendix.

3 DATA PROCESSING

The data were reduced using the ATNF Spectral Analysis Package (ASAP)⁵ and fit using the Continuum and Line Analysis Single-dish Software (CLASS)⁶ package, using standard procedures as described in the respective manuals.

3.1 Data Reduction

ASAP is a new software package developed by the ATNF to reduce single-dish single-pointing spectral lines observations, with particular application to the ATNF suite of telescopes.

During the reduction procedure, the data were read into ASAP, an *auto_quotient*⁷ was applied, as well as a first order polynomial before the data were frequency-aligned. The data were then averaged over time and polarisation, the gain

elevation correction was applied, as was an opacity correction of 10 per cent (priv. communication J. Reynolds). The rest frequency was then set (23.694512 and 23.7226336 GHz for the NH_3 (1,1) and NH_3 (2,2) transitions, respectively) and a third order polynomial was applied.

Comparison of the main hyperfine components V_{LSR} of the NH_3 (1,1) and NH_3 (2,2) transitions reveals a small velocity shift between the (1,1) and (2,2) spectra. The mean offset in velocity between the two transitions is 0.24 km/s with a standard deviation of 0.26 km/s. As mentioned in section 2, the expected resolution of these ammonia observations is 0.2 km/s. The rest frequencies, which were obtained from the Lovas catalogue, are believed to be less accurate than the velocity shift seen in our spectra.

3.2 NH_3 Fitting

Each of the NH_3 (1,1) and NH_3 (2,2) spectra were fit using the standard NH_3 (1,1) and NH_3 (2,2) methods, respectively, in CLASS. Under the assumption that each of the hyperfine components have equal excitation temperature and the same Gaussian velocity structure, these methods return the calculated flux density, rest velocity (V_{LSR}), linewidth (ΔV), & optical depth (τ) as well as the corresponding uncertainties to the fits for each source. A 3- σ cutoff was used to define non-detections for both transitions.

While the data quality is mostly of a high standard, a subset of the spectra show approximately sinusoidal variations in the baseline, typically with period 40–100 km s⁻¹. Attempting to use polynomial fitting to remove baseline variations with a similar velocity scale as the hyperfine structure (~ 50 km s⁻¹) may substantially alter the structure of the spectra. While the line V_{LSR} and ΔV are likely robust (the line width of the main component and satellites are typically much smaller than the baseline variations), the ratios of measured flux density, both for the hyperfines within a transition and between different transitions, are not. Derived optical depths and temperatures should therefore be treated with caution for these sources. Any spectra showing this anomaly are flagged as BR (baseline ripple) in column 11 of Table 1. Some sources, particularly those towards the Galactic centre, show multiple blended velocity components, making the fits less reliable. These data are flagged as BL (Blended) in column 11 of Table 1. All other spectra are considered reliable and marked as an R in this column.

The parameters derived from the fits to both the NH_3 (1,1) and NH_3 (2,2) spectra are given in Table 1. The source name is given in column 1, in right ascension order, using names consistent with Hill et al. (2005). The source class is given in column 2. Columns 3, 4, 5 and 6 present the flux density, V_{LSR} , linewidth (ΔV) and the optical depth for the NH_3 (1,1) transition. Columns 7–10 present these parameters for the NH_3 (2,2) transition. For sources with an NH_3 (1,1) detection but no NH_3 (2,2) detection, a 3- σ upper limit is derived from the NH_3 (2,2) spectra which is given in column 7, and no values are listed in columns 8–10.

Column densities and rotational temperatures were derived in the standard way (e.g. Ungerechts et al. 1986). The kinetic temperature estimates were calculated from the rotational temperature following the procedure outlined in Tafalla et al. (2004). The derived molecular gas properties for each source are presented in Table 2, in right ascen-

³ The CABB hardware was originally developed for the Australia Telescope Compact Array (ATCA) and was also used in the DFB3 backend at Parkes. See <http://www.narrabri.atnf.csiro.au/observing/CABB.html>

⁴ see <http://www.parkes.atnf.csiro.au/observing/documentation/software/CORREL/index.html>

⁵ <http://www.atnf.csiro.au/computing/software/asap/>

⁶ <http://www.iram.fr/IRAMFR/GILDAS/doc/html/class.html/class.html>

⁷ The ASAP *auto_quotient* command combines the nearest source and reference spectra, dividing and subtracting the latter off.

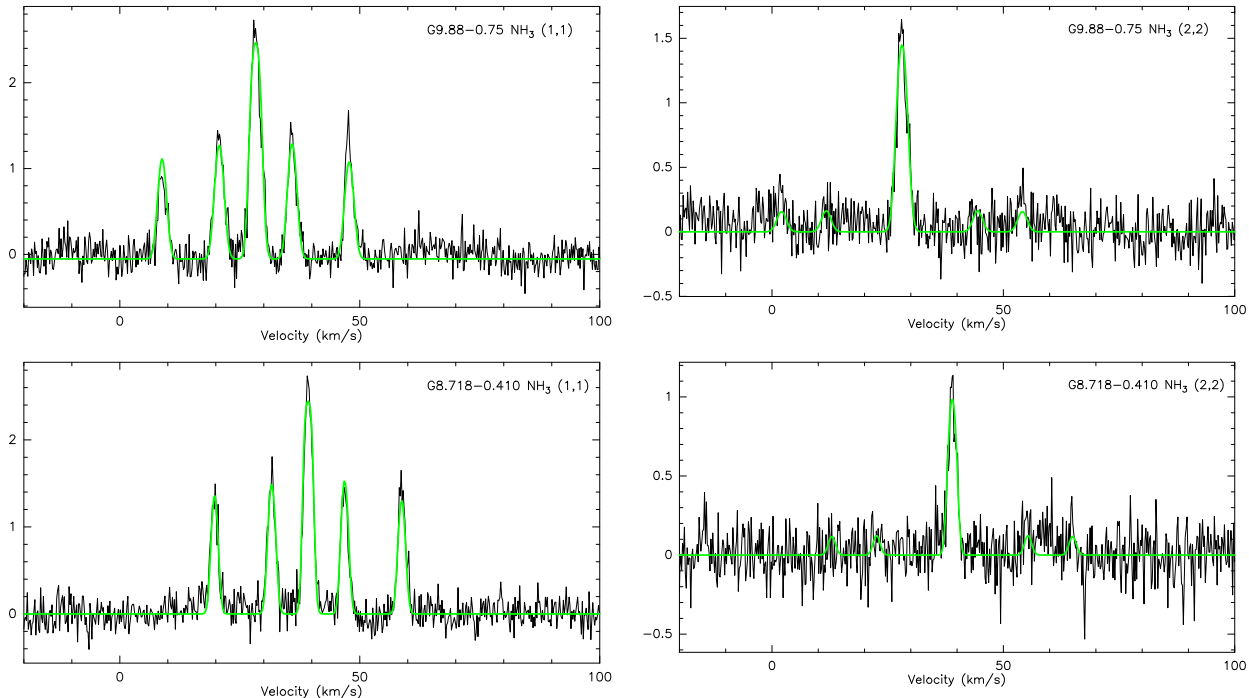


Figure 1. Sample $\text{NH}_3(1,1)$ and $(2,2)$ spectra, shown left to right, respectively. The y-axis is in units of Jy/beam. The green lines on the spectra indicate the fits as determined with CLASS. Top Row: G9.88-0.75 a class M (see section 2) source, and bottom: G8.718-0.410 a class MM source. The full set of $\text{NH}_3(1,1)$ and $(2,2)$ spectra can be found in the Appendix. Whilst a sample of the full appendix is included here (Fig. ??), the entire appendix of spectra can be found in the online version.

sion order. The rotational temperature (T_{rot}) and kinetic temperature (T_{kin}) are given in columns 2 and 5, with the lower and upper limits to each temperature given in columns 3 & 4 and 6 & 7, respectively. Temperature uncertainties are discussed further below. The column density of the $\text{NH}_3(1,1)$ ($N_{\text{NH}_3(1,1)}$) and the total column density of the gas ($N_{\text{NH}_3}^{\text{TOT}}$) are presented in columns 8 and 9, respectively.

Given the varying robustness of the $\text{NH}_3(1,1)$ and $(2,2)$ detections, sources were divided into 4 groups based on the reliability of the spectra (and hence derived physical properties). Group 4 sources were defined as those with no $\text{NH}_3(1,1)$ detection. No physical properties were derived for these sources, which can be found in Table 3. Sources with an $\text{NH}_3(1,1)$ detection, but with either i) no $\text{NH}_3(2,2)$ detection or ii) the $\text{NH}_3(1,1)$ & $(2,2)$ $V_{\text{LSR}}/\Delta V$ differed by >3 km/s (making it unlikely the emission is coming from the same gas) were defined as group 3. For these sources, there is no $\text{NH}_3(2,2)$ emission at the position of the $\text{NH}_3(1,1)$ detection, so the RMS of the $\text{NH}_3(2,2)$ spectra was used to derive an upper temperature limit and column density estimate. These numbers are highly uncertain. Group 2 sources are defined as those with both $\text{NH}_3(1,1)$ and $(2,2)$ detections which have consistent kinematics but the signal to noise of at least one spectra lies in the range $3 < \sigma < 10$. Finally, sources with both $\text{NH}_3(1,1)$ and $(2,2)$ detections $>10\sigma$ are defined as group 1. These group allocations are given in column 10 of Table 2.

Uncertainties in the temperature were estimated for group 1 and 2 sources using the uncertainties in the mea-

sured parameters (Flux density, V_{LSR} , ΔV & τ) from the fits to the spectra. For each core, a maximum and minimum rotational temperature were derived assuming each of the parameters was at 1σ above or below the actual measured value (e.g. $\text{Flux}^{11} + \Delta\text{Flux}^{11}$ or $\text{Flux}^{11} - \Delta\text{Flux}^{11}$). The lower and upper rotational temperatures are shown in columns 3 and 4 of Table 2. These extrema were then used to derive corresponding lower and upper limits to the kinetic temperatures, again following Tafalla et al. (2004). The lower and upper kinetic temperatures are shown in columns 6 and 7 of Table 2. As a general rule, the cores at low temperatures are well constrained, while those above ~ 20 K are poorly constrained. This is reflected in the larger error bars for poorly constrained temperatures, and is not unexpected given the insensitivity of $\text{NH}_3(1,1)$ and $(2,2)$ as a temperature probe of warmer gas (e.g. Danby et al. 1988).

For some sources (e.g. G305.776-0.251) the rotational temperature was so high that the analytic for determined by Tafalla et al. (2004) was no longer reliable. These sources have very small (<8 K) lower limits, and no upper limit could be derived.

3.3 Detection Rates

This Parkes ammonia $(1,1)$ and $(2,2)$ survey targeted a total of 244 sources of the 405 in the SIMBA sample of Hill et al. (2005), i.e., 60 per cent. The breakdown of the different classes of source targeted and their detection rates in both $\text{NH}_3(1,1)$ and $(2,2)$ is given in Table 4. Of the 244 sources observed, 138 sources were detected (at a $3\text{-}\sigma$ threshold) in $\text{NH}_3(1,1)$ (56 per cent) including two sources which

Table 2. Parameters derived from the $\text{NH}_3(1,1)$ and $\text{NH}_3(2,2)$ spectra. Sources are in right ascension order, as per Table 1.

Source	T_{rot}^a (K)	$T_{\text{rot}}^{\text{lower}}$ (K)	$T_{\text{rot}}^{\text{upper}}$ (K)	T_{kin}^a (K)	$T_{\text{kin}}^{\text{lower}}$ (K)	$T_{\text{kin}}^{\text{upper}}$ (K)	$N_{\text{NH}_3(1,1)}$ (10^{13}cm^{-2})	$N_{\text{NH}_3}^{\text{TOT}}$ (10^{14}cm^{-2})	Rel. Group $^\beta$
G269.15-1.13	28	18	63	42	22	-	5.9	0.7	1
G291.256-0.769	16	9	39	19	9	82	8.6	1.0	1
G291.256-0.743	22	19	28	29	22	41	8.3	0.9	1
G291.309-0.681	23	15	53	31	17	-	4.8	0.5	2
G291.576-0.468	< 22	-	-	< 22	-	-	4.5	0.5	3
G291.58-0.53	< 23	-	-	< 23	-	-	4.9	0.6	3
G294.97-1.7	< 16	-	-	< 16	-	-	4.3	0.5	3
G304.890+0.636	< 9	-	-	< 9	-	-	2.5	0.7	3
G305.145+0.208	< 14	-	-	< 14	-	-	4.3	0.6	3
G305.137+0.069	< 12	-	-	< 12	-	-	9.7	1.7	3
G305.192-0.006	20	12	45	25	13	119	11.7	1.3	1
G305.21+0.21	37	26	66	71	37	-	12.2	1.6	2
G305.197+0.007	14	10	22	16	11	28	15.6	2.1	2
G305.226+0.275	23	18	32	31	22	51	18.7	2.1	2
G305.228+0.286	35	23	66	62	30	-	16.6	2.0	2
G305.238+0.261	18	12	31	21	13	48	10.4	1.2	2
G305.248+0.245	< 13	-	-	< 13	-	-	8.1	1.2	3
G305.233-0.023	16	12	24	19	13	32	16.8	2.1	2
G305.269-0.010	15	13	17	17	15	20	19.1	2.5	1
G305.355+0.194	21	13	44	27	15	106	13.2	1.5	2
G305.37+0.21	< 16	-	-	< 16	-	-	13.4	1.7	3
G305.362+0.185	22	16	35	28	18	61	17.8	2.0	2
G305.361+0.151	< 26	-	-	< 26	-	-	2.5	0.3	3
G305.538+0.340	< 14	-	-	< 14	-	-	10.3	1.4	3
G305.55+0.01	23	13	79	30	14	-	5.4	0.6	2
G305.552+0.012	< 26	-	-	< 26	-	-	2.0	0.2	3
G305.561+0.012	29	18	80	44	21	-	3.2	0.3	2
G305.776-0.251	17	2	-	19	2	-	4.0	0.5	2
G305.81-0.25	22	16	37	28	18	69	9.4	1.0	2
G305.833-0.196	12	7	26	13	7	37	6.1	1.0	2
G306.33-0.3	< 8	-	-	< 8	-	-	6.5	2.0	3
G306.343-0.302	< 19	-	-	< 19	-	-	8.4	1.0	3
G309.917+0.494	< 14	-	-	< 14	-	-	8.6	1.2	3
G309.92+0.4	< 24	-	-	< 24	-	-	3.7	0.4	3
G318.92-0.68	24	16	43	33	19	104	13.0	1.4	2
G323.74-0.3	30	16	141	46	18	-	8.0	0.9	2
G332.646-0.647A	17	14	20	19	16	24	6.3	0.7	2
G332.646-0.647B	20	17	25	25	19	35	3.1	0.3	2
G332.695-0.609	< 10	-	-	< 10	-	-	15.6	3.1	3
G332.725-0.62	< 10	-	-	< 10	-	-	9.2	2.1	3
G332.627-0.511	17	12	28	19	13	41	6.4	0.8	2
G332.827-0.552	18	12	32	22	13	52	16.0	1.9	1
G0.331-0.164	< 7	-	-	< 7	-	-	12.3	4.9	3
G0.310-0.170	< 10	-	-	< 10	-	-	11.7	2.6	3
G0.32-0.20	23	15	38	29	18	74	11.0	1.3	2
G1.105-0.098	32	27	40	53	39	83	5.8	0.7	1
G1.13-0.11	30	28	34	47	40	58	6.3	0.7	1
G0.549-0.868	16	13	20	18	14	25	6.5	0.9	1
G0.627-0.848	< 11	-	-	< 11	-	-	13.4	2.4	3
G0.600-0.871	13	5	53	14	5	221	9.7	1.4	2
G2.54+0.20	12	9	19	13	9	23	10.6	1.7	1
G5.504-0.246	12	9	16	13	9	19	9.4	1.6	2
G5.90-0.42	16	12	23	18	13	30	18.9	2.4	2
G5.90-0.44	23	16	40	30	18	84	10.2	1.1	2
G8.111+0.257	29	18	76	44	21	-	1.8	0.2	2
G8.127+0.255	17	13	27	20	14	38	7.2	0.9	2
G8.138+0.246	17	13	26	20	14	36	8.2	1.0	2
G8.13+0.22	15	12	18	16	13	21	11.9	1.6	1
G5.948-1.125	< 9	-	-	< 9	-	-	2.7	0.7	3
G5.962-1.128	13	4	-	14	4	-	5.2	0.8	2
G5.975-1.146	21	15	35	26	17	61	6.1	0.7	2
G5.971-1.158	< 12	-	-	< 12	-	-	5.3	0.9	3
G9.63+0.19	27	19	44	38	22	110	19.2	2.2	2
G8.68-0.36	12	11	14	13	11	16	38.9	6.2	2

Table 2. Cont.

Source	T_{rot}^a (K)	$T_{\text{rot}}^{\text{lower}}$ (K)	$T_{\text{rot}}^{\text{upper}}$ (K)	T_{kin}^a (K)	$T_{\text{kin}}^{\text{lower}}$ (K)	$T_{\text{kin}}^{\text{upper}}$ (K)	$N_{\text{NH}_3(1,1)}$ (10^{13}cm^{-2})	$N_{\text{NH}_3}^{\text{TOT}}$ (10^{14}cm^{-2})	Rel. Group $^\beta$
G8.686-0.366	16	13	20	19	15	24	35.6	4.5	2
G8.644-0.395	11	8	15	11	8	17	9.9	1.9	2
G8.713-0.364	9	8	10	9	8	11	23.3	6.2	1
G8.735-0.362	12	9	17	13	10	20	17.6	2.8	2
G8.724-0.401	10	7	13	10	7	14	20.1	4.6	1
G8.709-0.412	11	9	14	12	9	16	15.9	2.9	1
G8.718-0.410	13	10	16	14	11	18	19.8	3.0	2
G10.287-0.110	22	15	42	29	16	93	18.9	2.1	2
G10.284-0.126	25	17	40	33	20	86	17.4	2.0	2
G10.288-0.127	19	16	25	23	18	34	10.7	1.3	1
G10.29-0.14	17	14	21	20	16	26	15.5	1.9	1
G10.343-0.142	16	11	27	19	12	38	14.3	1.8	2
G10.32-0.15	24	16	45	33	18	120	13.0	1.4	2
G10.359-0.149A	26	23	29	37	31	44	3.3	0.3	1
G10.359-0.149B	25	22	29	35	28	45	4.2	0.5	1
G10.63-0.33B	38	20	157	75	25	-	15.1	1.9	2
G10.62-0.33	17	13	24	20	14	31	19.2	2.4	2
G10.62-0.38	42	33	61	98	54	-	5.5	0.7	1
G9.88-0.75	14	12	18	16	12	21	18.8	2.6	2
G10.620-0.441	13	10	18	14	10	21	9.3	1.4	2
G11.075-0.384	< 9	-	-	< 9	-	-	12.9	3.2	3
G11.11-0.34	17	12	27	20	12	38	20.6	2.5	2
G11.117-0.413	11	9	13	12	10	14	12.1	2.2	1
G12.88+0.48	23	15	40	30	17	84	14.7	1.7	2
G12.914+0.493	22	8	-	29	8	-	2.9	0.3	2
G11.903-0.140	12	9	16	12	9	18	21.2	3.6	1
G11.93-0.14	< 12	-	-	< 12	-	-	13.4	2.1	3
G12.112-0.125	< 12	-	-	< 12	-	-	5.2	0.8	3
G11.942-0.256	19	12	33	23	13	55	18.0	2.1	2
G12.18-0.12A	14	12	17	15	13	19	16.4	2.3	1
G12.216-0.119	17	13	25	20	14	35	9.4	1.1	1
G12.43-0.05	15	9	34	16	9	59	5.7	0.7	2
G12.68-0.18	13	11	16	14	11	18	29.0	4.4	2
G11.94-0.62B	11	10	12	12	11	13	24.7	4.5	1
G11.93-0.61	12	12	13	13	12	15	26.1	4.1	1
G12.722-0.218	< 15	-	-	< 15	-	-	9.8	1.3	3
G12.855-0.226	16	13	21	19	14	27	19.8	2.5	2
G12.885-0.222	13	10	18	14	10	21	19.0	2.9	2
G12.892-0.226	11	9	12	11	10	13	21.4	4.1	1
G12.90-0.25B	11	10	12	12	11	12	27.8	5.2	1
G12.859-0.272	22	14	42	28	16	97	16.4	1.8	2
G13.87+0.28	40	2	-	86	2	-	1.6	0.2	2
G12.90-0.26	14	12	17	16	13	20	35.5	4.8	2
G12.878-0.226	< 9	-	-	< 9	-	-	24.4	6.0	3
G12.897-0.281	14	10	21	16	11	27	28.2	3.9	2
G12.914-0.280	< 9	-	-	< 9	-	-	27.3	6.4	3
G12.938-0.272	< 9	-	-	< 9	-	-	16.1	3.7	3
G11.49-1.48	< 12	-	-	< 12	-	-	7.0	1.1	3
G14.60+0.01	31	18	96	50	21	-	16.3	1.9	2
G10.84-2.59	22	12	86	27	14	-	2.6	0.3	2
G16.580-0.079	< 10	-	-	< 10	-	-	8.2	1.6	3
G16.58-0.05	14	12	18	16	13	22	9.8	1.3	1
G18.30-0.39	29	15	109	43	18	-	6.1	0.7	2
G19.61-0.1	32	19	122	52	23	-	4.9	0.6	2
G16.871-2.154	14	13	17	16	14	19	28.8	3.9	2
G16.86-2.15	13	10	18	14	11	21	18.3	2.7	1
G22.36+0.07B	< 10	-	-	< 10	-	-	10.0	2.0	3
G23.71+0.17	14	11	18	15	12	22	15.7	2.2	2
G23.43-0.18	< 7	-	-	< 7	-	-	19.8	9.0	3
G23.268-0.257A	24	19	33	32	22	55	3.1	0.3	3
G23.409-0.228	12	9	16	12	9	18	18.6	3.2	2
G23.754+0.095	< 14	-	-	< 14	-	-	8.8	1.2	3
G29.96-0.02B	16	11	26	18	12	37	13.4	1.7	2
G29.912-0.045	14	12	18	16	13	21	22.8	3.0	1

Table 3. Sources which were observed in NH₃(1,1) and (2,2) but are non-detections (group 4 sources) or are too confused to fit.

Source Name	Class ^{a, b, c}	Source Name	Class ^{a, b, c}
G269.45-1.47	MR ND	G305.519-0.040	MM ND
G270.25+0.84	M ND	G305.520-0.020	MM ND
G284.271-0.391	MM ND	G305.549+0.002	MM M
G284.295-0.362	MM ND	G305.581+0.033	MM ND
G284.307-0.376	MM ND	G305.605+0.010	MM M/ND
G284.338-0.417	MM ND	G306.319-0.343	MM ND
G284.35-0.42	M M/ND	G318.913-0.162	R ND
G284.345-0.404	MM ND	G330.952-0.18	MR M
G284.341-0.389	MM M/ND	G332.640-0.586	MM D/M
G284.328-0.365	MM ND	G332.701-0.587	MM ND
G284.384-0.441	MM M/ND	G332.777-0.584	MM M/ND
G284.344-0.366	MM ND	G332.794-0.598	MM ND
G284.352-0.353	MM ND	G0.204+0.051	MM SB
G287.37+0.65	M ND	G0.49+0.19	M SA [?]
G290.40-2.91	M ND	G0.266-0.034	MM SB
G291.27-0.70	MR D	G0.21-0.00	MR SB
G291.288-0.706	MM ND	G0.497+0.170	MM SA [?]
G291.302-0.693	MM M	G0.240+0.008	MM SB
G290.37+1.66	M M/ND	G0.527+0.181	R SA [?]
G291.587-0.499	MM ND	G0.271+0.022	MM SB
G291.572-0.450	MM M/ND	G0.257+0.011	MM SB
G291.608-0.532	MM ND	G0.83+0.18	M M/ND
G291.597-0.496	MM ND	G0.325-0.242	MM ND
G291.630-0.545	MM ND	G1.124-0.065	MM SB
G291.614-0.443	MM ND	G1.134-0.073	MM SB
G293.824-0.762	MM ND	G1.14-0.12	M S [?]
G293.82-0.74	MR M	G0.55-0.85	MR SB
G293.892-0.782	MM D/ND	G5.48-0.24	R ND
G293.95-0.8	MR ND	G6.53-0.10	R M/ND
G293.942-0.876	MM ND	G6.60-0.08	M M/ND
G293.989-0.936	MM M/ND	G6.62-0.10	MM ND
G294.52-1.6	M M/ND	G5.97-1.17	R ND
G294.945-1.737	MM ND	G10.10+0.72	R ND
G294.989-1.720	M ND	G9.966-0.020	MM M/ND
G298.26+0.7	M D/ND	G9.99-0.03	M ND
G299.02+0.1	M ND	G10.001-0.033	R ND
G299.024+0.130	MM ND	G10.44-0.01	M D/ND
G300.455-0.190	MM ND	G9.924-0.749	MM ND
G300.51-0.1	M ND	G11.948-0.003	MM ND
G301.14-0.2	MR ND	G12.02-0.03	M D/ND
G302.03-0.06	MR D/ND	G11.902-0.100	MM M/ND
G304.906+0.574	MM M/ND	G11.861-0.183	MM ND
G304.919+0.542	MM ND	G11.942-0.157	MM D/M
G305.952+0.555	MM ND	G12.200-0.003	MM D/M
G304.952+0.522	MM M/ND	G11.956-0.177	MM ND
G304.933+0.546	MM ND	G11.99-0.27	M M
G304.942+0.550	MM ND	G19.607-0.234	MR ND
G305.201+0.241	MM M	G19.70-0.27A	M ND
G305.202+0.230	MM D/M	G16.883-2.188	MM D/M
G305.20+0.02	R ND	G21.87+0.01	MR ND
G305.200+0.02	M ND	G24.450+0.489	MM ND
G305.242+0.225	MM ND	G23.420-0.235	MM M
G305.513+0.333	MM D/ND	G23.319-0.298	MM S [?]
G305.533+0.360	MM ND	G29.853-0.062	MM ND

^a Denotes the source class. See Section 2.

^b Code indicates whether the source is: ND – non-detection; M – may be a detection, these sources are typically weak and/or the spectrum is too noisy to positively confirm a detection; D – detection too weak compared with the noise; S – Strong detection in which either (B) the hyperfines are blended and can't be fit or (A) has absorption features or (?) the spectrum is confused with multiple components and a fit will not converge.

^c Two codes appear in this column only if the NH₃(2,2) transition is not in agreement with the NH₃(1,1), with the former following the latter and separated by a '/'.

could not be fit (see Table 3). These tended to be sources quite close to the Galactic Centre and whose spectra displayed very broad lines with a combination of hyperfine blending, multiple lines and/or absorption features. A further 11 sources had detections that were too weak ($< 3\sigma$) in NH₃(1,1) and a further 24 sources are possible detections though the noisy spectrum and very low signal-to-noise

Table 4. Summary of NH₃ detections

Class	Sources Targeted	Good Fits (1,1)	(2,2)	% of NH ₃ (1,1) with (2,2)
Total	244	138 (56%)	102 (42%)	74%
MM	148	79 (53%)	54 (36%)	68%
M	54	35 (65%)	27 (50%)	75%
MR	24	12 (50%)	12 (50%)	100%
R	18	12 (67%)	9 (50%)	75%
M+MR+R	96	59 (61%)	48 (50%)	81%

makes it difficult to determine whether there is a detection or not.

Three of the sources targeted have multiple velocity components in their spectra: G10.359-0.149; G23.268-0.257 and G332.646-0.647 which are visible in both the NH₃(1,1) and (2,2) transition, though G23.268-0.257B did not pass our cuts described in section 3.2. For nine sources, the strength of the (2,2) transition is stronger than that of the (1,1), indicating that these sources are likely the hottest in the sample. It is not possible to determine an accurate column density or temperature for these sources, which are annotated by a † in Table 1. These sources do not represent one particular class of source. As these transitions were observed simultaneously we can rule-out weather effects causing this.

4 RESULTS

In this section the results pertaining to the parameters obtained from fitting the NH₃(1,1) and (2,2) spectra (i.e., ΔV , τ , V_{LSR} , Flux density) are discussed, as well as the parameters derived from the fits: T_{kin} , NH₃(1,1) column density ($N_{\text{NH}_3(1,1)}$) and total NH₃ column density ($N_{\text{NH}_3}^{\text{TOT}}$). Table 5 presents the mean and median values of each of these parameters.

4.1 Linewidth ΔV

The linewidth of the sample ranges from 1.1 to 7.1 kms^{-1} for the NH₃(1,1) transition and 1.3 to 9.2 kms^{-1} for the NH₃(2,2) transition. The mean linewidth of the NH₃(1,1) data is 2.9 kms^{-1} , with a standard deviation of 1.2 kms^{-1} , whilst the (2,2) transition displays a slightly broader mean linewidth of 3.1 kms^{-1} , with a standard deviation of 1.7 kms^{-1} .

Pillai et al. (2006) found linewidths between 0.8 and 3 kms^{-1} for their sample of nine infrared dark clouds (IRDCs), whilst for their sample of methanol maser selected sources, Longmore et al. (2007) find linewidths between 0.7 and 4.6 kms^{-1} . Both the linewidths of these authors and our sample, which is comprised of a cross-section of star-forming sources, display linewidths that are greater than those reported by Jijina et al. (1999) for their sample of low mass cores. Pillai et al. (2006) attribute the larger linewidths of their sample to velocity dispersions and turbulence. Churchwell et al. (1990) find an average NH₃ linewidth of 3.1 kms^{-1} for their sample of UC HII regions, whilst Sridharan et al. (2005) find a median linewidth of 1.5 kms^{-1} for their sample of high mass starless cores and 1.9 kms^{-1} for high mass protostellar objects. Sridharan et al. (2005) interpret the linewidth difference between the different types

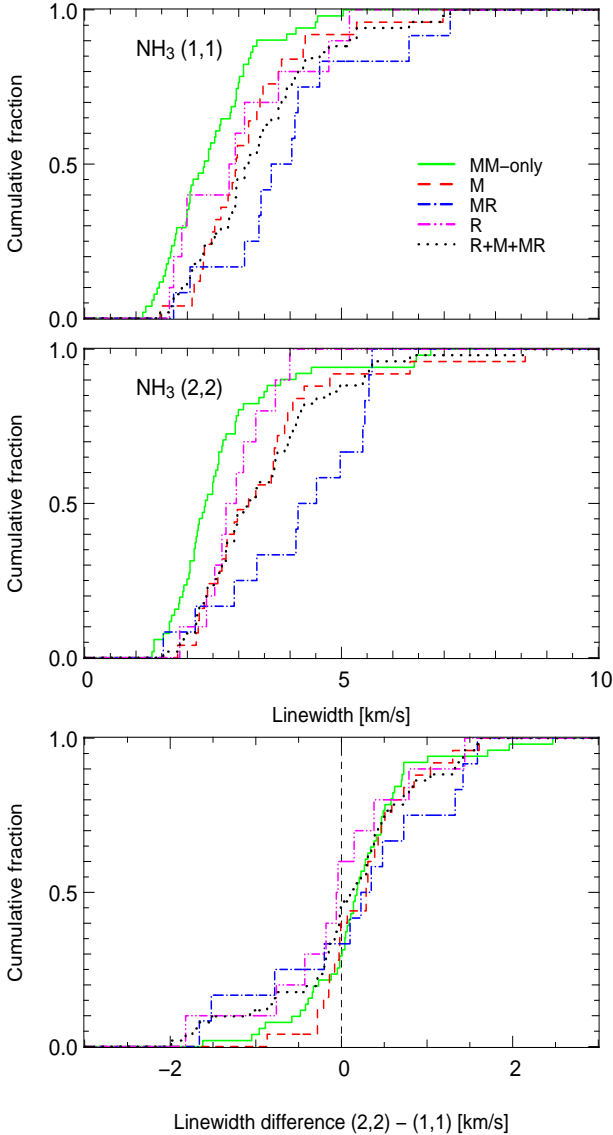


Figure 2. Cumulative distribution of the $\text{NH}_3(1,1)$ (top) and $\text{NH}_3(2,2)$ (middle) linewidths of the sample. Key is as on plot. There is a slight offset between the (1,1) and (2,2) transitions.

of source as an indication of evolutionary status, with more quiescent and less evolved cores having smaller linewidths.

The cumulative distribution plots of the $\text{NH}_3(1,1)$ and $\text{NH}_3(2,2)$ linewidth (see Fig. 2), with respect to the class of source in the sample, confirms that the MM-only sources have the narrowest linewidths of the sample. Class R sources are confined to a small region of the linewidth parameter space which may simply reflect the small number of sources in this sample (see Table 4). For both the $\text{NH}_3(1,1)$ and (2,2) distributions, the maser sample traces that of the sample with active star formation (class M+MR+R) indicating that masers are ubiquitous tracers of massive star formation. Class MR sources have the broadest linewidths of the sample, given that they have two indicators of active star formation they could potentially be warmer and/or more evolved.

To test the hypothesis that two, or more, classes

of source are drawn from the sample parent population, Kolmogorov-Smirnov (KS) tests were performed. For both the (1,1) and (2,2) transition, the KS-tests for the individual classes were inconclusive which is likely due to the low number of sources in the individual samples of active sources (M, MR and R). When comparing the MM-only sample (class MM) with the star formation sample (class M+MR+R), the statistics become significant enough to perform robust KS tests. The null hypothesis, that the samples are drawn from the same population, can clearly be rejected when comparing the MM-only sample (class MM) with the star formation sample (class M+MR+R) - see full red and dotted black line in Fig. 2. This results holds for both the (1,1) and (2,2) transition, with probabilities smaller than 10^{-3} and 7×10^{-5} , respectively.

As the $\text{NH}_3(1,1)$ and (2,2) transition are expected to be emitted from the same gas, we would then expect that they display similar linewidths. The top two panels of Figure 2 suggest that there is a slight increase in linewidth with an increase in the NH_3 transition. Note that the $\text{NH}_3(1,1)$ plot includes all sources, whilst the $\text{NH}_3(2,2)$ plot includes sources with a Rel. Group equal to 1 or 2, as Group 3 sources have only upper limits for this transition. This result is in agreement with Pillai et al. (2006) who also found that for some of their IRDCs the (2,2) linewidths were slightly larger than the (1,1) linewidths, which they interpreted to mean that each transition was not exactly tracing the same gas. Broader $\text{NH}_3(2,2)$ linewidths, with respect to the $\text{NH}_3(1,1)$ linewidth, could be interpreted as internal heating, but further (mapping) observations of these sources are necessary to examine this.

The bottom panel of Figure 2 is a plot of the difference between the $\text{NH}_3(1,1)$ and (2,2) linewidth. This panel places the top and middle panel in context, indicating that approximately half of the sources have broader (2,2) linewidths and the other half have less broad line widths compared with the $\text{NH}_3(1,1)$ transition. This panel also clearly shows that each of the classes of source have comparable (2,2) versus (1,1) linewidths. If we refer to the sources for which we have robust detections (i.e. a Rel. Group equal to 1 or 2), the (2,2) linewidths can vary from -2.0 to 2.5 kms^{-1} broader than the (1,1) transition with a median and mean of 0.0 kms^{-1} .

For the 45 per cent of sources with $\text{NH}_3(1,1)$ linewidths broader than the (2,2) transition, the (2,2) linewidth is 50 to 99 per cent that of the width of the (1,1) transition, with a median of 90 per cent of the (1,1) linewidth. The small difference in linewidth ensures that we can use the two transitions to determine the temperature of the cores.

Thermal linewidths range from 0.1 to 0.4 kms^{-1} with a median of 0.2 kms^{-1} , as calculated from the NH_3 derived kinetic temperature. The turbulence is clearly dominating for all sources, including the MM-only where the linewidth is the smallest.

4.2 Optical Depth τ

The optical depth of the sample ranges from 0.1 to 3.8 for the $\text{NH}_3(1,1)$ transition and from 0.1 to 9.4 for the (2,2) transition. We caution however that this lower limit is simply the minimum value for optical depth as determined from CLASS, and should simply be interpreted as optically-thin emission. The median optical depth of the $\text{NH}_3(1,1)$ is 1.4

compared with 0.1 for the (2,2) transition. These optical depth values are consistent with Longmore et al. (2007) who found that the majority of their maser sources have optical depths between 0.3 and 5. There is no obvious difference in the optical depth between the different classes of source for either of the NH_3 transitions. Only 22 per cent of sources observed in both (1,1) and (2,2) have greater optical depths for the (2,2) transition.

4.3 V_{LSR}

The V_{LSR} of the sample ranges from -87.8 to 113kms^{-1} . There are no trends between the source V_{LSR} and type of source in the sample.

4.4 Flux Density

The $\text{NH}_3(1,1)$ flux density of the sample ranges from 0.3 to 11.60 Jy/beam, both of which are MM-only sources, with a median of 2.4 Jy/beam. The different classes of source in the sample display a similar range of flux. Class M, MM and MR have similar median flux density values of 2.5 Jy/beam, whilst class R have a median flux of 1.6 Jy/beam, though the sample of active star formation sources (class M, MR and R) has a median value of 2.4 Jy/beam. For nine sources, the flux density of the (2,2) transition is greater than that of the (1,1) – see section 3.3.

For the $\text{NH}_3(2,2)$ transition the flux density of the sample ranges from 0.3 to 6.4 Jy/beam, with a median of 1.2 Jy/beam. Each of the four classes of source display similar flux ranges for this transition. The median $\text{NH}_3(2,2)$ flux density of each class suggests that the MM-only sources are not as bright as the other classes of source. We caution however that this difference is small. The $\text{NH}_3(2,2)$ flux density of the MM-only cores is 75 per cent that of the sample with active star formation.

Cumulative distributions and Komolgorov-Smirnov (KS) tests indicate that there is little difference between each of the classes in terms of their flux density.

The peak line intensity of the $\text{NH}_3(2,2)$ transition for our sources is on average 40 per cent that of the (1,1) transition (excluding the nine sources which have greater (2,2) flux densities). This ratio is in excellent agreement with Pillai et al. (2006) who also find that for their sample of IRDCs, the peak intensity of the (2,2) is 40 per cent that of the (1,1).

4.5 Kinetic Temperature T_{kin}

The kinetic temperature of the sample ranges from 9.0 to 98.0 K, with a median of 20 K. Despite such a large temperature range, only 22 per cent of sources have temperatures greater than 30 K, whilst only 6 per cent have temperatures in excess of 50 K. 78 per cent of sources are cooler than 30 K. As discussed in section 3.2 and 5.3, the lower transition (1,1) and (2,2) NH_3 data are useful as a thermometer when the temperature is less than 30 K (Danby et al. 1988). When the temperature is greater than this, these transitions can not support accurate temperature determinations. Tafalla et al. (2004) are more conservative and suggest that $\text{NH}_3(1,1)$ and (2,2) actually poorly constrain temperatures

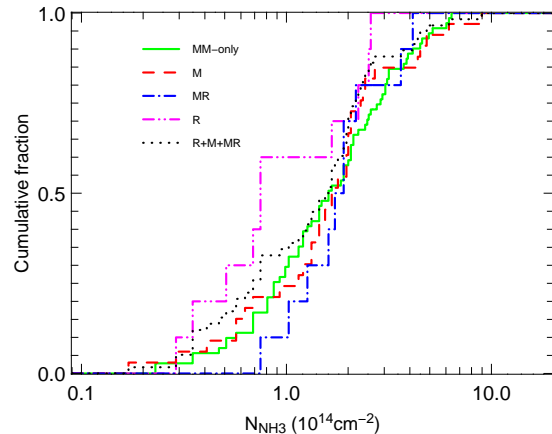


Figure 3. Cumulative distribution of the column density of the different classes in the sample. Key is on the plot.

greater than 20 K. However, our method of modelling, i.e., Bayesian inference, factors in the larger error bars for ill constrained temperatures, when deriving masses from SEDs – see section 5.2.2.

The MM-only sources are cooler on average than each of the individual classes comprising maser and/or radio continuum associations as well as the sample of active star formation (class M+MR+R) – see Table 5. The cumulative distribution plot of the temperature is discussed in detail in section 5.1.

Pillai et al. (2006) found that the temperature of their IRDC sample range from 11–17 K, whilst Churchwell et al. (1990) find approximately half of their UC HII sample to range between 15 and 25 K and the other half to have temperatures in excess of 25 K.

4.6 Total Column Density

The total column density of the sources, derived from both the $\text{NH}_3(1,1)$ and (2,2) transitions, ranges from 0.3 to $15.7 \times 10^{14} \text{ cm}^{-2}$, with a median column density of $2.8 \times 10^{14} \text{ cm}^{-2}$. Figure 3 presents the cumulative distribution plot of the column density. The radio sample (class R) has the lowest column density on average compared with the other classes – see Table 5.

4.7 Correlations

Cross-correlating each of the parameters discussed in the aforementioned sections reveals very few trends and thus relationships between them. There is a slight correlation between the flux and the optical depth of a sources, with an increase in flux translating to an increase in the optical depth of the source.

Both Longmore et al. (2008) and Pillai et al. (2006) found that the $\text{NH}_3(1,1)$ linewidth and kinetic temperature of a sources are correlated, with an increase in one leading to an increase in the other. Longmore et al. (2008) found that when they compared these two parameters, the NH_3 -only cores of their sample – those without methanol maser associations – were confined to a small and distinct region in the plot, which was clearly separate from the parameter

space occupied by the methanol maser sources. The NH_3 -only sources were cooler than the maser sources, yet of comparable linewidth.

As mentioned in section 4.1, Pillai et al. (2006) found that IRDCs in their sample have greater linewidths than the low-mass stars in the sample of Jijina et al. (1999). Additionally, they find that their IRDCs are colder relative to the sample of Jijina et al. (1999) and the UC HII sample of Churchwell et al. (1990). A comparison of their IRDCs with more evolved examples of massive star formation (e.g. UC HII regions and high mass protostellar objects e.g. Beuther et al. 2002) reveals the IRDCs to be cooler than these sources and to have narrower linewidths on average.

We do not see this correlation in our own data, i.e., the MM-only sources are not distinct from the other star-formation classes with respect to their temperature. Instead, we find that the MM-only sample has comparable temperatures to sources with a methanol maser and/or radio continuum sources, coupled with smaller linewidths. The eight dark clouds for which we have $\text{NH}_3(1,1)$ and $(2,2)$ observations are not confined to cooler temperatures or smaller linewidths as per Pillai et al. (2006), nor is there a trend between their $\text{NH}_3(1,1)$ linewidth and T_{kin} . The lack of correlation between the $\text{NH}_3(1,1)$ and T_{kin} of our sample may be attributed to two factors. Firstly, our data are likely subject to beam dilution with low-resolution (58 arcsec), compared with the 40 arcsec resolution of Pillai et al. (2006) and the interferometric observations (< 11 arcsec) of Longmore et al. (2008). Additionally the combination of $\text{NH}_3(1,1)$ and $(2,2)$ provides reliable temperatures up to ~ 30 K, so we are insensitive to the greater temperature range coverage of Longmore et al. (2008) who used higher transition ammonia data to determine their temperatures.

While Longmore et al. (2006) were able to probe warmer regions better than us, due to higher transition NH_3 data which they also measured, when it comes to the cold sources of particular interest here, this is not an issue. Both studies are sensitive to probing the temperature in the coldest gas, where only the $(1,1)$ and $(2,2)$ lines are significantly excited.

5 ANALYSIS

5.1 Previous SED modelling

Hill et al. (2009) performed spectral energy distribution modelling of ~ 180 sources of the SIMBA sample (see section 1), using the Bayesian inference method of fitting (e.g. Pinte et al. 2008). This method of fitting considers the potential correlations between parameters to produce quantitative estimates of the range of validity of key parameters (temperature, mass, luminosity) extracted from SED fitting. As the modelling procedure is outlined in detail in section 3.1 of Hill et al. (2009) we simply summarise the procedure here.

The sources were modelled according to a two-component model which denotes a central warm core surrounded by a cold dust envelope. The hot component of this model is assumed to radiate as a blackbody whilst the cold component accounts for optically thin emission from the dust (see Equation 1, Hill et al. 2009). The sources were

then fit for four free parameters: R_{hot} , T_{hot} , T_{cold} and M_{cold} . Those sources without mid-infrared emission (i.e. a hot component) were fit for the cold component only and thus two free parameters: T_{cold} and M_{cold} .

It was clear from SED modelling (Hill et al. 2009) that an absence of far-infrared data, where the peak of the dust emission lies, hinders accurate determinations of the source temperature. Additionally as the mass and luminosity of a source are highly correlated with that of the temperature, assessing the evolutionary status of a source from SED fitting alone is difficult. Greater observational constraints were necessary in order to facilitate further SED fitting and analysis.

5.2 SED modelling revisited

5.2.1 Comparison of temperature derivation methods

These ammonia data provide an independent, and more accurate, determination of the source temperature. Following the assumption that the kinetic temperature is equivalent to the dust temperature, it is then possible to revisit our previous SED modelling. Li et al. (2003) showed that the gas temperature of their sources i.e., the kinetic temperature as derived from NH_3 observations, was within a few K of the dust temperature. According to their observations, T_{kin} and T_{dust} are expected to be similar in cold regions. Schnee & Sargent (2007) also find excellent agreement between the dust and gas temperature of their star less core in Taurus. Contrary to this, both Molinari et al. (1996) and Sridharan et al. (2002) find discrepancies when comparing dust temperatures and kinetic temperatures derived from NH_3 . However, both these authors derived their dust temperatures from *IRAS* data which is subject to poor resolution and the emission is likely optically thick. When the dust is highly optically thick large differences between the gas and dust temperatures can occur (Kruegel & Walmsley 1984). Molinari et al. (1996) themselves caution that *IRAS* fluxes alone are insufficient for proper estimates of the dust temperature.

Of the ~ 180 sources that were originally SED modelled (Hill et al. 2009), 82 were also observed with ammonia, though 30 of these sources only have upper limits to their temperature. Figure 4 compares the kinetic temperature (T_{kin}) of each source, as derived from the NH_3 observations, with the dust temperature as estimated from our previous SED modelling (T_{SED}). This figure contains the 52 source with reliable continuum and ammonia observations for estimating both temperatures (Rel. Group 1 and 2, in Table 2), thus allowing a statistical comparison of both methods. The red line on the plot indicates where T_{SED} and T_{kin} are equal.

Figure 4 shows that there are no systematic biases introduced in either of the methods used to determine the temperature estimates. If SED fitting was biasing the resultant temperature of a core, then these data would all be above, or below, the red line. The SED method, although not strongly constraining the temperature, appears a robust method for obtaining a first order unbiased estimate of the core temperature. In this section, we perform the SED modelling again, this time using the kinetic temperature as derived from NH_3 .

Table 5. Mean and median as derived from the ammonia spectra for each of the source classes. For a breakdown of the number of sources within each class, refer to Table 4.

Parameter		Class				whole sample	all except MM-only (M+MR+R)
		MM-only (MM)	maser (M)	maser+radio (MR)	radio (R)		
Flux Den. ^{1,1} (Jy/beam)	mean	3.3	3.0	2.9	2.2	3.1	2.8
	median	2.6	2.6	2.5	1.6	2.5	2.4
$\Delta V^{1,1}$ (km.s ⁻¹)	mean	2.6	3.1	3.4	3.0	2.8	3.1
	median	2.3	2.9	3.5	2.4	2.7	3.0
Flx Den. ^{2,2} (Jy/beam)	mean	1.3	1.5	1.3	1.0	1.3	1.4
	median	1.1	1.5	1.2	0.9	1.2	1.3
$\Delta V^{2,2}$ (km.s ⁻¹)	mean	2.6	3.5	3.9	2.7	3.0	3.5
	median	2.3	3.3	4.1	2.7	2.6	3.2
T_{kin} (K)	mean	22.4	29.8	32.2	28.5	25.8	30.2
	median	19.0	25.0	24.0	23.5	20.0	25.0
$N_{\text{NH}_3}^{\text{TOT}}$ (10^{14}cm^{-2})	mean	3.4	3.7	3.5	2.2	3.4	3.4
	median	2.7	2.9	3.2	1.3	2.8	2.9

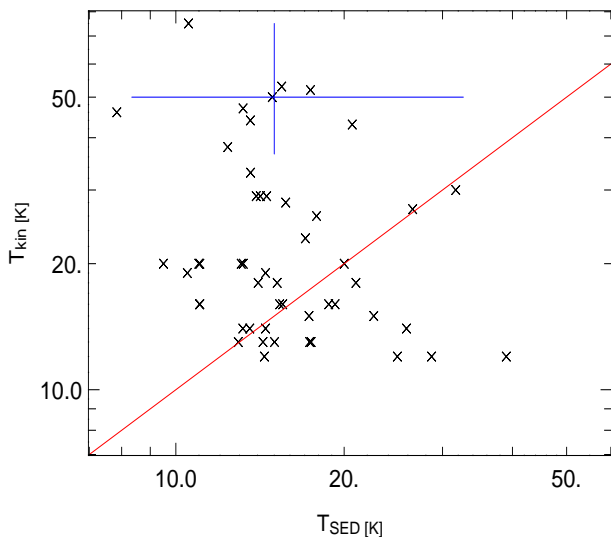


Figure 4. Comparison of the temperature as derived from SED modelling with that derived from the NH_3 observations. The red line indicates where these two parameters would be equal. The error bars are indicated by the blue lines.

5.2.2 SED modelling with NH_3

SED modelling was performed using the Bayesian inference method, following the procedure summarised above (section 5.1) and outlined in Hill et al. (2009, section 3). Rather than fitting for the temperature (T_{cold}), we fixed the dust temperature to the kinetic temperature, as derived from NH_3 , and fit solely for the mass of the source (as well as the hot parameters, for those sources with mid-infrared data), assuming the same dust properties used previously. As per Hill et al. (2009) we have assumed the near distance for all sources with a distance ambiguity.

The probability distributions of the temperature were set to Gaussian distributions defined by the value of, and uncertainties with, the NH_3 temperature (T_{kin}) - see Table 1. For those sources where only an upper limit value to

the temperature has been determined (Rel. Group 3) we assume a uniform probability distribution between 2.73 K and the upper limit. The estimated range of validity for the mass and the luminosity derived from this method then not only accounts for the uncertainty on the temperature but also considers the correlations between parameters.

Figure 5 is a plot of the probability curves for the temperature and mass of a source, comparing our previous SED fitting method (Hill et al. 2009), with that of the SED fitting performed in this paper using NH_3 derived temperatures. Figure 5 illustrates how kinetic temperatures allow tighter constraints on the mass of a source, as is expected. This source, G10.288-0.127 a MM-only source with no mid-infrared association which was consequently fit with a single cold component, corresponds to the bottom row of Fig. 1 of Hill et al. (2009). This source was chosen to illustrate how a source with limited sampling of the SED can be well constrained by known or constrained temperatures. It is clear that the NH_3 data (red curve) provides greater constraints on the temperature (left-hand plot), especially for those sources with few data points, compared with deriving the temperature from SED fitting (black curve). The range of validity for the temperature is now constrained to a smaller portion of the parameter space. It is clear that accurate temperatures are necessary to derive accurate sources masses.

5.3 SED results

Table 6 presents the range of validity for the temperature, mass and luminosity of each of the 52 sources which were re-modelled using their NH_3 temperature in the SED fits. The cumulative distribution plots of the temperature, mass and luminosity are presented in Figure 6. Note that all sources, regardless of their reliability flag (Table 2) were included in this Figure.

An interesting result evident from the probability distributions of all of the sources re-modelled is the complementarity of the SED fitting and NH_3 observations in terms of parameter determinations. Even when the uncertainty on

Table 6. Parameters resulting from SED modelling of 52 SIMBA sources with NH_3 temperatures reported in Table 2. For each of the temperature, mass and luminosity, the range corresponding to a 1-sigma (68 per cent) probability of occurrence is presented, with the $_{min}$ and $_{max}$ values representing the lower and upper values of this range, respectively.

Source Name	Ident tracer	Fit Type	Temperature		Mass		Luminosity	
			$T_{\text{cold}_{min}}$ K	$T_{\text{cold}_{max}}$ K	M_{min} M_{\odot}	M_{max} M_{\odot}	L_{min} L_{\odot}	L_{max} L_{\odot}
G305.833-0.196	mm	SINGLE	26	28	7.6E+01	1.0E+02	3.7E+03	1.6E+04
G323.74-0.3	m	SED	15	37	2.0E+02	2.8E+03	5.3E+03	1.0E+05
G0.32-0.20	mr	SINGLE $^{\alpha}$	17	31	3.3E+03	8.7E+03	3.4E+04	6.7E+05
G1.105-0.098	mm	SINGLE $^{\alpha}$	28	47	5.3E+02	1.4E+03	1.0E+05	9.8E+05
G1.13-0.11	r	SED $^{\alpha}$	34	47	3.1E+02	3.8E+03	4.6E+05	1.4E+06
G0.549-0.868	mm	SINGLE $^{\alpha}$	15	24	2.5E+01	5.0E+01	6.1E+01	5.3E+03
G0.600-0.871	mm	SINGLE $^{\alpha}$	11	42	1.9E+01	1.3E+02	8.9E+01	7.2E+04
G2.54+0.20	m	SINGLE	17	26	2.0E+02	4.6E+02	5.7E+02	2.4E+04
G5.504-0.246	mm	SINGLE $^{\alpha}$	10	19	1.9E+03	5.0E+03	8.3E+02	3.4E+04
G5.90-0.42	m	SED $^{\alpha}$	15	29	5.3E+02	1.9E+03	5.3E+03	7.2E+04
G8.111+0.257	mm	SINGLE $^{\alpha}$	21	83	6.1E+00	3.3E+01	5.7E+02	6.7E+05
G8.127+0.255	mm	SINGLE $^{\alpha}$	14	32	5.7E+01	2.0E+02	2.7E+02	5.0E+04
G8.138+0.246	mm	SINGLE $^{\alpha}$	15	31	1.1E+02	4.0E+02	5.7E+02	7.2E+04
G8.13+0.22	mr	SED $^{\alpha}$	14	20	9.3E+02	2.5E+03	3.7E+03	3.4E+04
G5.962-1.128	mm	SINGLE $^{\alpha}$	8	31	8.1E+00	7.6E+01	6.6E+00	1.6E+04
G5.975-1.146	mm	SINGLE $^{\alpha}$	17	50	7.1E+00	2.5E+01	1.9E+02	7.2E+04
G9.63+0.19	mr	SED $^{\alpha}$	16	36	2.0E+02	1.1E+03	2.5E+03	5.0E+04
G8.68-0.36	mr	SINGLE $^{\alpha}$	11	16	6.6E+03	1.1E+04	3.7E+03	3.4E+04
G8.686-0.366	m	SINGLE $^{\alpha}$	16	23	1.1E+03	2.2E+03	5.3E+03	7.2E+04
G10.287-0.110	mm	SINGLE $^{\alpha}$	12	35	5.7E+01	3.1E+02	2.7E+02	7.2E+04
G10.284-0.126	m	SED $^{\alpha}$	18	45	4.3E+01	2.3E+02	1.2E+03	3.4E+04
G10.288-0.127	mm	SINGLE $^{\alpha}$	19	32	2.8E+01	6.6E+01	3.9E+02	1.6E+04
G10.29-0.14	mr	SED $^{\alpha}$	16	25	2.7E+02	7.1E+02	3.7E+03	2.4E+04
G10.343-0.142	m	SINGLE $^{\alpha}$	15	35	5.0E+01	1.5E+02	2.7E+02	5.0E+04
G10.63-0.33B	mm	SINGLE $^{\alpha}$	16	62	1.7E+02	1.2E+03	1.1E+04	4.3E+06
G10.62-0.33	m	SED $^{\alpha}$	14	28	9.3E+02	3.8E+03	5.3E+03	7.2E+04
G9.88-0.75	r	SED $^{\alpha}$	13	20	1.2E+03	3.3E+03	2.5E+03	1.6E+04
G10.62-0.38	mr	SINGLE $^{\alpha}$	12	32	6.6E+03	3.5E+04	2.4E+04	2.1E+06
G11.11-0.34	r	SED $^{\alpha}$	13	28	8.1E+02	3.8E+03	3.7E+03	7.2E+04
G11.117-0.413	mm	SINGLE $^{\alpha}$	11	14	4.6E+02	8.1E+02	8.9E+01	3.7E+03
G12.88+0.48	m	SINGLE $^{\alpha}$	14	28	9.3E+02	3.3E+03	1.7E+03	1.0E+05
G12.914+0.493	mm	SINGLE $^{\alpha}$	9	36	5.7E+01	4.6E+02	8.9E+01	7.2E+04
G11.903-0.140	mr	SINGLE $^{\alpha}$	9	17	5.3E+02	1.6E+03	1.3E+02	1.1E+04
G12.18-0.12A	m	SINGLE $^{\alpha}$	14	19	2.5E+03	4.3E+03	3.7E+03	3.4E+04
G12.216-0.119	mm	SINGLE $^{\alpha}$	16	31	2.2E+03	5.7E+03	2.4E+04	6.7E+05
G12.43-0.05	r	SED	16	30	2.2E+03	8.7E+03	1.1E+04	3.2E+05
G12.68-0.18	m	SED $^{\alpha}$	11	17	1.9E+03	4.3E+03	2.5E+03	1.1E+04
G11.94-0.62B	mm	SINGLE $^{\alpha}$	11	13	1.6E+03	2.5E+03	5.7E+02	5.3E+03
G11.93-0.61	mr	SED $^{\alpha}$	13	15	1.6E+03	3.3E+03	1.7E+03	7.7E+03
G12.90-0.25B	mm	SINGLE $^{\alpha}$	11	12	7.1E+02	1.1E+03	1.9E+02	3.7E+03
G13.87+0.28	m	SED	10	39	4.6E+02	6.6E+03	7.7E+03	3.2E+05
G12.859-0.272	mm	SED $^{\alpha}$	15	40	1.3E+02	8.1E+02	1.2E+03	3.4E+04
G12.90-0.26	m	SED $^{\alpha}$	14	19	1.6E+03	3.8E+03	5.3E+03	2.4E+04
G14.60+0.01	mr	SED $^{\alpha}$	11	31	1.3E+02	9.3E+02	3.9E+02	1.1E+04
G10.84-2.59	r	SINGLE $^{\alpha}$	12	30	1.3E+02	6.1E+02	1.9E+02	3.4E+04
G16.58-0.05	m	SED $^{\alpha}$	14	21	8.1E+02	2.2E+03	2.5E+03	1.6E+04
G18.30-0.39	r	SED	14	36	1.7E+02	1.4E+03	5.3E+03	7.2E+04
G19.61-0.1	m	SED $^{\alpha}$	13	36	1.3E+02	1.1E+03	5.7E+02	5.0E+04
G16.86-2.15	m	SED $^{\alpha}$	11	17	8.1E+02	2.2E+03	8.3E+02	3.7E+03
G23.71+0.17	r	SED $^{\alpha}$	12	20	1.6E+03	5.0E+03	7.7E+03	7.2E+04
G29.96-0.02B	mr	SED $^{\alpha}$	13	31	2.2E+03	1.0E+04	1.1E+04	4.6E+05
G29.912-0.045	mm	SINGLE $^{\alpha}$	14	20	1.9E+03	3.8E+03	3.7E+03	5.0E+04

$^{\alpha}$ denotes those sources that were fit with *IRAS* upper limits - see Hill et al. (2009).

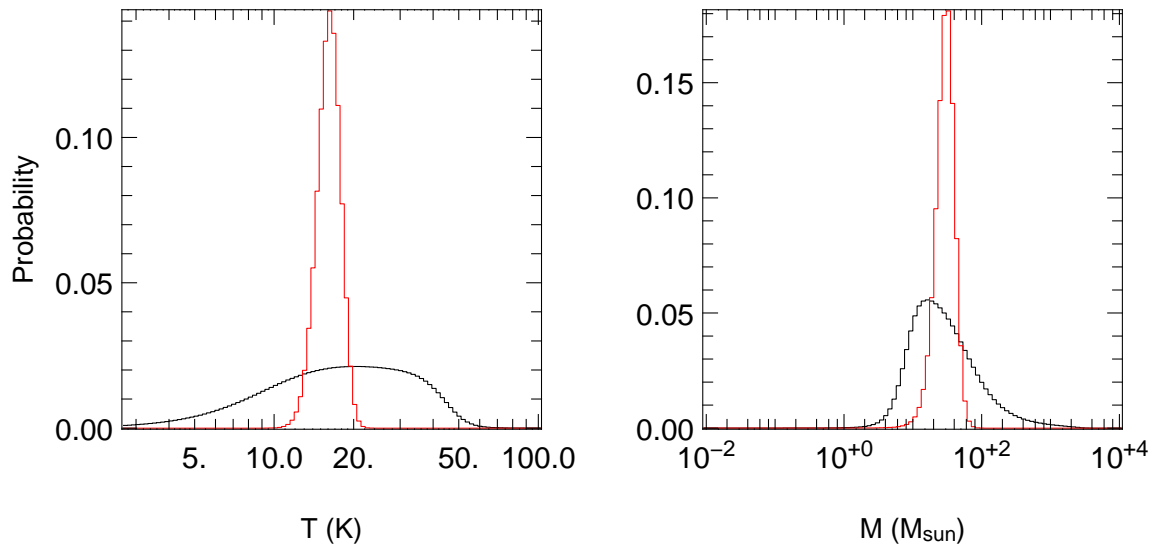


Figure 5. The probability curves of one source (G10.288–0.127, corresponding to the bottom row of Fig. 1 Hill et al. 2009) comparing the two SED methods. The black line indicates the probability curve corresponding to a SED fit temperature (Hill et al. 2009) whilst the red probability curve is indicative of the probability when the temperature is fixed using the ammonia derived T_{kin} . As can be seen, constraints on the temperature translate as tighter probability curves for parameters resulting from SED modelling, i.e., mass.

the kinetic temperature derived from NH_3 is large, the constraints from the SED fitting and the NH_3 analysis are very complementary. SED modelling provides good constraints on the upper limit of the temperature when the ammonia data are ill-constrained due to the absence of higher transitions (see section 3.2). On the other hand, NH_3 provides good constraints on the lower limit to the temperature when the ambiguities from SED modelling become very large.

Comparison of the temperature-fit probability curves (Hill et al. 2009) with those of the probability curves produced here, indicates that, in most instances, the mass probability peaks in the same place for both methods. In all instances, the probability curve of the mass for each individual source is more tightly constrained using the NH_3 temperatures, as is demonstrated in Fig. 5.

The cumulative distribution plot of the temperature (Fig. 6, left) suggests that class MM sources are slightly cooler than the other classes of source. This difference reflects the fact that 9 of the 11 sources in Rel. Group 3, and thus sources with upper limits, are MM-only sources which effectively add a ‘bump’ to the MM-only curve at low temperatures. However, the difference between the MM-only sources and those with signatures of massive star formation is not statistically significant, with a KS test probability of 0.4. If we do not include the sources in Rel. Group 3, the distribution of the temperature shows little distinction between the different classes of source in the sample for this parameter with a KS probability of 0.98.

The cumulative distribution plot of the mass (Fig. 6, middle) indicates that the MM-only sources are the least massive of the sample, whilst class MR are the most massive. The difference in the mass is more significant than for the temperature, though the KS test, with a probability of 0.08, does not allow us to rule on the null hypothesis that MM-only sources are drawn from the same population as that star formation sources. This is likely a result of the relatively small number of sources modelled.

The cumulative distribution plot of the luminosity (Fig. 6, right) reveals the MM-only sources to be marginally less luminous than the other classes of source, which is not surprising given that the mass and luminosity are correlated and the temperature of the sources is slightly smaller.

5.4 Luminosity vs Mass Diagram

As per Hill et al. (2009), we have drawn a luminosity vs. mass (hereafter $M - L$ diagram) diagram for the sources which we have re-modelled with SEDs. André et al. (2000) proposed that the $M - L$ diagram was a useful diagnostic tool for class 0 and class I low-mass protostars, which provides insight into a source’s evolutionary status. Hill et al. (2009) showed that care should be taken with interpretation of $M - L$ diagrams drawn from SEDs.

Due to the low number of sources which were re-modelled in each class of source, little distinction can be discerned for the different classes of source nor can proposed evolutionary tracks be drawn from this diagram. The $M - L$ diagram can be found in Figure 7.

5.5 Determining a mass for NH_3 sources not SED modelled

Of the 138 sources deemed to have good $\text{NH}_3(1,1)$ fits reliable kinetic temperatures were derived for 128 (see section 3.3). Of these 128 only 52 NH_3 sources were originally SED modelled by us. Consequently, only 52 NH_3 sources have enough information to draw spectral energy distributions and determine their mass.

Assuming that the NH_3 temperature is equivalent to that of the dust temperature (Li et al. 2003; Schnee & Sargent 2007), we can estimate the mass of the remaining sources which have reliable NH_3 and millimetre continuum data. Here we ignore sources which are lacking millimetre continuum or distance information.

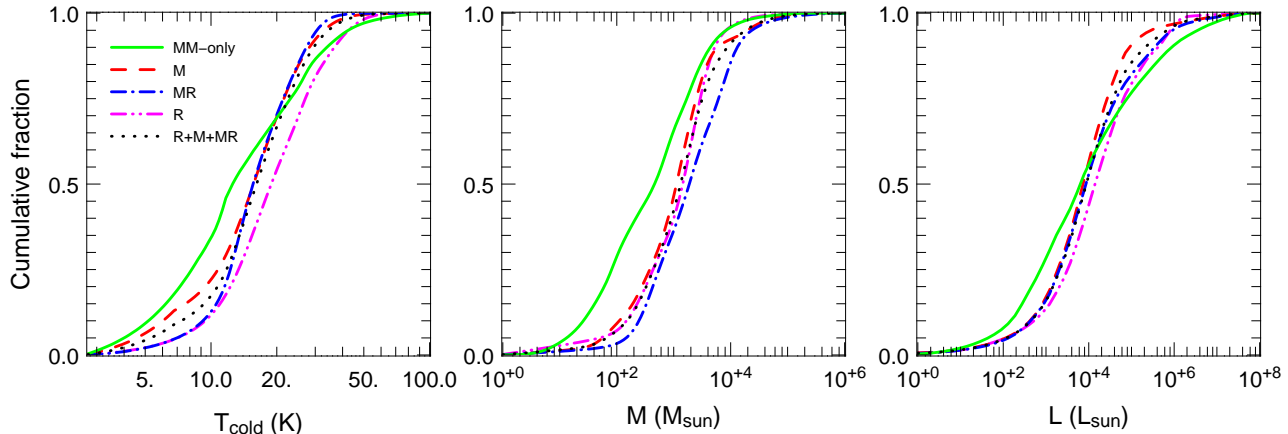


Figure 6. Cumulative distributions for the SIMBA sources that were re-modelled with SEDs using their NH_3 temperature. The key on the left plot indicates the different classes of source in the sample. left: distribution of temperature. middle: distribution of mass. right: distribution of luminosity.

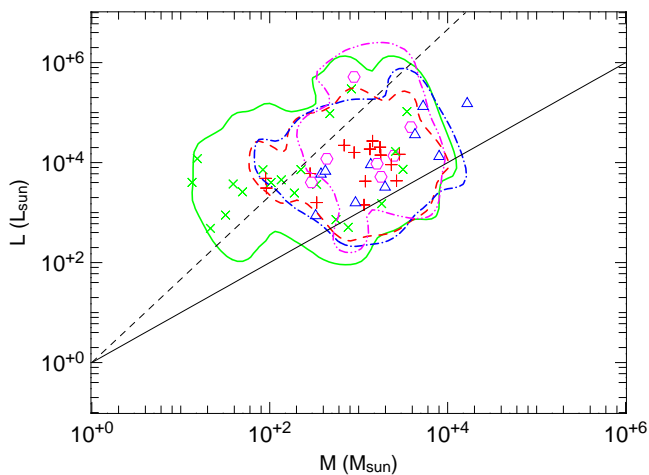


Figure 7. Mass-Luminosity diagram for the different classes of source in the sample. Each of the points represents the median value (*i.e.* the values at which the cumulative probability distribution is 0.5) of the mass and luminosity of the individual sources (green cross: mm, red plus sign: m, blue triangles: mr and pink circles: r). The contour levels represent the regions enclosing 68 per cent of the Bayesian probability for a given class of sources (green full line: mm, red dashed line: m, blue dot-dash line: mr and pink dot-dot-dash line: r). The full and dashed straight lines depict the $M = L$ and $M = L^{0.6}$ relations, respectively. The same figure can be found in Hill et al. (2009, Fig. 3) for sources which were previously SED modelled.

The 65 NH_3 sources for which we derive a mass from their NH_3 temperature, according to the procedure outlined in section 4.1, and equation 1, of Hill et al. (2005), are presented in Table 7. Sources which have reliable temperature information and an estimate of the error associated with the temperature have both a minimum and maximum estimation of the mass in columns 3 and 4. Those sources for which a mass was derived from an upper limit temperature value do not have a temperature range and are lacking values in these columns. These masses should be treated with caution and are an estimate of the mass only.

Though the mass drawn from this method is derived solely from the millimetre continuum flux, rather than a

SED sampled at various wavelengths, it provides a useful approximation to the source mass in the absence of further data. Hill et al. (2005) showed that the contribution of free-free emission to the millimetre flux is expected to be negligible compared with the dust emission. We recognise the potential for contributions from free-free emission that may be missed from the interferometric survey (Walsh et al. 1998) used to draw these conclusions and we caution interpretation of these results (*cf.* Longmore et al. 2009).

6 DISCUSSION

6.1 Physical properties of the clumps

Previous work has shown the MM-only cores of our sample to be excellent candidates for young massive protostars. Their characteristic physical properties, such as temperature and mass, suggested that these objects are indicative of the earliest stages of massive star formation. These conclusions, which were drawn from (sub)millimetre continuum emission observations and spectral energy distribution modelling, are not without their caveats. SED modelling is subject to ambiguities and is heavily reliant on well constrained temperatures in order to produce a reliable mass estimate. In addition, it is not yet known whether the MM-only core is indeed forming massive stars.

Using the kinetic temperatures as derived from this NH_3 line study, we are now in a position to ascertain which physical properties of the MM-only cores are similar to those of sources with known star formation activity, and which physical properties differ.

Analysis, in the previous sections, has revealed the MM-only class to have smaller NH_3 linewidths on average than class M, MR and R - those sources with a methanol maser and/or radio continuum association. This is true for both ammonia transitions. SED modelling, using the Bayesian inference method, in conjunction with well constrained kinetic temperatures, as derived from ammonia, reveals the MM-only cores to be the least massive of the sample.

Interestingly, class MM sources display many similarities in the distributions of the other physical parameters

Table 7. Mass of the 65 NH₃ cores that could not be SED modelled. A minimum and maximum mass are determined from the errors on the temperature (see Table 1). For those sources in Rel. group 3 an error on the temperature could not be obtained, and in this instance there is no corresponding error on the mass given in this table. In a few instances, no physically meaningful maximum temperature could be derived, and these sources will not have a minimum mass in this table.

Name	M	M _{min}	M _{max}
G269.15-1.13	4.0e+02	1.8e+01	1.0e+03
G291.256-0.769	4.6e+02	9.0e+01	1.6e+03
G291.256-0.743	5.3e+02	3.4e+02	7.2e+02
G291.309-0.681	6.1e+02	8.1e+01	1.4e+03
G291.576-0.468	1.1e+03	–	–
G291.58-0.53	4.3e+03	–	–
G294.97-1.7	1.5e+02	–	–
G305.145+0.208	1.3e+02	–	–
G305.137+0.069	5.3e+02	–	–
G305.192-0.006	2.3e+02	4.5e+01	6.4e+02
G305.197+0.007	4.6e+02	2.3e+02	8.6e+02
G305.21+0.21	5.3e+02	1.2e+01	1.3e+03
G305.226+0.275	1.1e+02	6.7e+01	1.8e+02
G305.228+0.286	9.3e+00	2.5e-01	2.3e+01
G305.238+0.261	3.1e+02	1.2e+02	6.6e+02
G305.248+0.245	4.6e+02	–	–
G305.233-0.023	1.0e+02	5.5e+01	1.8e+02
G305.269-0.010	6.1e+02	5.1e+02	7.6e+02
G305.362+0.185	3.5e+02	1.4e+02	6.2e+02
G305.361+0.151	3.1e+02	–	–
G305.37+0.21	9.3e+02	–	–
G305.55+0.01	1.1e+02	–	3.4e+02
G305.552+0.012	2.0e+02	–	–
G305.561+0.012	2.7e+02	–	6.7e+02
G305.776-0.251	1.1e+02	–	5.6e+04
G305.81-0.25	9.3e+02	3.7e+02	1.8e+03
G306.33-0.3	1.1e+02	–	–
G306.343-0.302	3.8e+01	–	–
G309.917+0.494	1.3e+02	–	–
G309.92+0.4	1.4e+03	–	–
G318.92-0.68	1.7e+02	4.9e+01	3.5e+02
G332.695-0.609	1.9e+03	–	–
G332.725-0.62	3.1e+02	–	–
G332.627-0.511	1.0e+02	3.8e+01	1.7e+02
G0.331-0.164	2.5e+03	–	–
G0.310-0.170	5.3e+02	–	–
G0.627-0.848	5.0e+01	–	–
G5.90-0.44	3.5e+02	1.2e+02	7.1e+02
G5.948-1.125	6.6e+01	–	–
G5.971-1.158	8.7e+01	–	–
G8.644-0.395	2.7e+02	1.3e+02	4.5e+02
G8.713-0.364	1.1e+03	7.8e+02	1.4e+03
G8.735-0.362	1.1e+03	5.7e+02	1.6e+03
G8.709-0.412	4.0e+02	2.8e+02	7.1e+02
G8.724-0.401	2.3e+02	1.4e+02	4.6e+02
G8.718-0.410	8.7e+01	6.1e+01	1.3e+02
G10.32-0.15	1.5e+02	3.9e+01	3.5e+02
G10.620-0.441	3.5e+02	2.1e+02	6.4e+02
G11.075-0.384	1.1e+03	–	–
G11.93-0.14	3.5e+02	–	–
G11.942-0.256	2.0e+02	7.0e+01	4.3e+02
G12.112-0.125	3.3e+03	–	–
G12.722-0.218	6.1e+02	–	–
G12.885-0.222	1.7e+02	9.5e+01	2.9e+02
G12.892-0.226	1.5e+02	1.2e+02	1.8e+02
G12.878-0.226	2.0e+02	–	–
G12.897-0.281	8.7e+01	4.6e+01	1.6e+02

Table 7 – continued

Name	M	M _{min}	M _{max}
G12.914-0.280	1.7e+02	–	–
G12.938-0.272	1.5e+02	–	–
G11.49-1.48	5.3e+02	–	–
G16.580-0.079	4.0e+02	–	–
G22.36+0.07B	2.5e+03	–	–
G23.43-0.18	1.3e+04	–	–
G23.409-0.228	1.2e+03	6.6e+02	1.9e+03
G23.754+0.095	3.1e+02	–	–

compared with the other classes of source. They have similar luminosities, NH₃ flux densities hence brightness level, and column densities as the other classes. The simultaneous analysis of the NH₃ and continuum data shows that the distribution of the temperature (Fig. 6) for the MM-only sources is not very distinct from that of the other classes, i.e., those with known star formation activity, but seems to extend to slightly smaller temperatures.

6.2 Are they gravitationally bound?

From SED modelling, it is clear that both NH₃ and continuum observations provide complementary constraints on SED derived source parameters. Even if each of these constraints, taken individually, provide limited information on the nature of the cores, the combination of these constraints reveal several trends that give insight into the cores and their evolutionary status: Class MM are smaller (Hill et al. 2005), less massive and more quiescent (smaller turbulent linewidths) than cores with signatures of star formation.

With this information, we can ascertain the gravitational equilibrium of the various classes of source in the sample. A plot presenting the virial mass $M_{\text{virial}} = \Delta V^2 R/G$, as a function of the gas mass derived from continuum observations (i.e. SIMBA), $M_{\text{continuum}}$, is presented in Fig. 8. This plot contains all sources which have a reliability flag (Rel. Group) of 1 or 2 in Table 2, though as a check, by including the sources with a reliability flag of 3, the correlation coefficient and the line of best fit do not differ significantly.

As can be seen in Fig 8, there is a strong correlation between the virial mass and gas mass of a source, with a correlation coefficient of 0.74. As the continuum mass of a source increases so too does the virial mass. Interestingly, the distribution of the virial parameter is very similar for the MM-only sources and the active star formation sample (class M+MR+R) suggesting a very similar gravitational state, despite the lower masses of the MM-only sources.

The virial parameter $\alpha = M_{\text{virial}}/M_{\text{continuum}}$ (Bertoldi & McKee 1992) has a median value of 0.95 (see Fig. 8, right panel), suggesting that the clumps are virialised. The precise value must be interpreted with caution given the uncertainties on both the virial mass (in particular on the size of the clumps) and on the continuum mass (e.g. uncertain dust emissivities), but it is clear that the clumps, on average, do not differ significantly from being virialised.

There is however a distribution of the virial parameter as a function of the source mass, ranging from ≈ 0.1 to ≈ 10 . The virial mass appears to vary as $M_{\text{virial}} \propto M_{\text{continuum}}^{0.6}$, in-

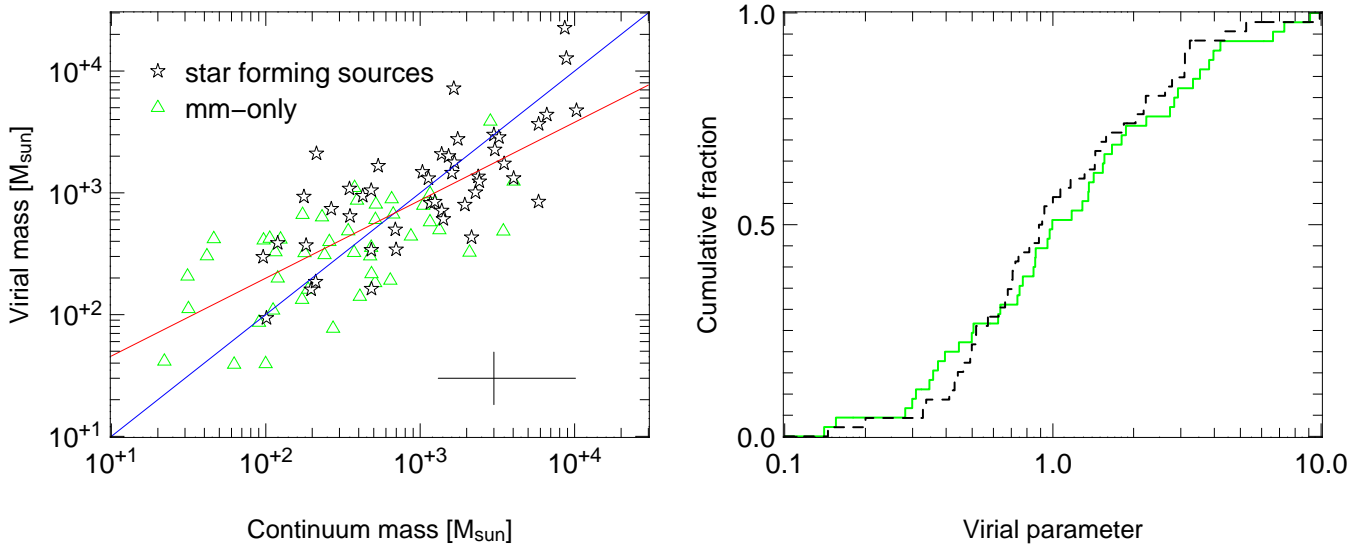


Figure 8. Left: The virial mass of the source as a function of the continuum mass. The blue line is where the two masses are equal, whilst the red line is the fit to the data, which has a correlation co-efficient of 0.74. The average error bars are as indicated on the plot, assuming a conservative 50 per cent error on the radius. Right: The cumulative distribution of the virial parameter. Same colour scheme as used in the left-hand plot.

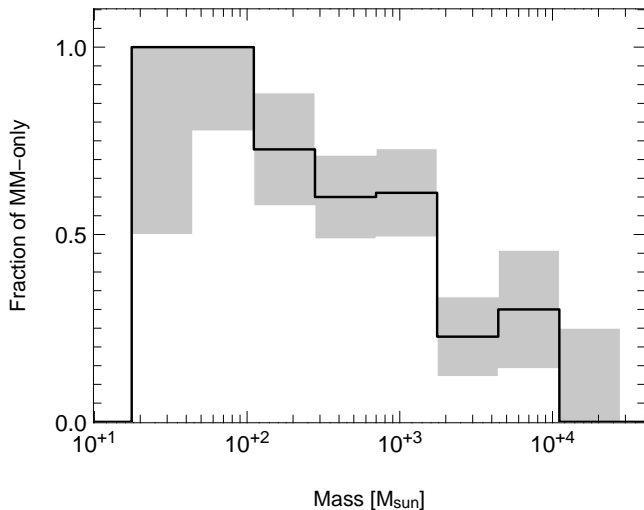


Figure 9. Fraction of MM-only sources as a function of the mass of the object. The error bars are identified by the grey boxes.

dicating that the more massive clumps are slightly more gravitationally bounded. This translates as a slightly larger median virial parameter of 1 for the MM-only cores, compared with the star forming sources (median $\alpha = 0.9$).

6.3 MM-only sources in the context of massive star formation

High-mass prestellar cores, or high-mass starless cores, the precursors of high-mass protostars in an analogous scaled-up version of low-mass starless cores, are still a missing piece of the high-mass star formation puzzle. Whether they may exist will serve to constrain competing massive star formation theories which propose coalescence and accretion as possible formation mechanisms. Infrared dark clouds (Jackson et al. 2008) have been proposed as possible candidates to host such

starless objects. However, high-angular resolution observations of a small sample of candidate massive starless cores have systematically revealed embedded, accreting protostars inside (e.g. Pillai et al. 2006).

We have identified a new class of source, the MM-only core, which are excellent candidates for early stage protostars or massive young stellar objects. SED analysis here reveals the MM-only sources to have a similar mass range, with a larger number of less massive sources, compared to the star forming sources, and very similar physical properties as these sources. The similar distribution of the virial state of equilibrium suggests that the MM-only sources are just as likely to form stars. These results suggest that the MM-only sources may in fact be scaled down objects compared with the star forming sources. The smaller mass, radii and linewidths of the MM-only cores further suggests that they will possibly form intermediate mass stars rather than high-mass stars.

Alternatively, the MM-only cores may not produce stars, and could remain starless transient clumps (e.g. Beuther & Henning 2009; Buckle et al. 2009). Further spectral line observations designed to ascertain the chemistry of the MM-only core are currently underway.

6.4 Is the MM-only population comprised of sub-samples?

It is also possible that the MM-only clumps could be comprised of multiple sub-samples or populations, with one interpretation that each of these sub-populations likely follow different evolutionary paths. In this instance, they could be comprised of both cores with high and low mass stars, cores which are in the very earliest stages of evolution, and also possibly some cores that are not destined to beget high mass stars.

Attempts to break class MM sources into multiple populations with respect to the mass, radius, linewidth, lumi-

osity and temperature reveal the MM-only population to have a continuous distribution with respect to each of these parameters (see for instance Fig. 6, 7 and 8). Consequently, there is currently no physical indication that the MM-only sources are comprised of distinct sub-populations.

Despite this, from our results we can infer that the MM-only sources will have different star formation histories depending on their initial mass. Figure 9 presents a plot of the fraction of MM-only sources as a function of the mass of the clump. All of the sources in our sample less than $100M_{\odot}$, are MM-only sources, and the fraction of objects that do not show any signature of star formation decreases as the mass of the clump increases.

This indicates that the most massive clumps have a higher efficiency to form massive stars. Additionally it may suggest that there is a dichotomy in mass around $100\text{--}200M_{\odot}$ for the MM-only sample. The MM-only sources below this threshold will likely not form massive stars.

Assuming an initial mass function (IMF) as per Chabrier (2003), and a star formation efficiency of 50 per cent, then we would need a minimum clump mass of $\approx 500M_{\odot}$ in order to support the formation of one star in excess of $10M_{\odot}$. That is, the maximum mass of the original clump dictates the size of stars that can form. Thus, clumps with masses lower than $100M_{\odot}$ will not form massive stars, whilst more massive MM-only sources on the contrary have enough material to form stars in excess of $10M_{\odot}$.

Assuming that the evolution of protostellar objects is faster for more massive objects could explain why we detect a smaller fraction of MM-only sources i.e. before signatures of star formation, for increasingly massive objects. In this instance, the MM-only cores do represent targets of choice to assess the earliest stages of star formation.

7 CONCLUSIONS

We have undertaken an ammonia molecular line study, in the lowest two inversion transitions, of young massive star formation regions in the southern hemisphere as part of an effort to characterise the earliest stages of high-mass star formation. The sample targeted was derived from the millimetre continuum emission studies of Hill et al. (2005, 2006) and included sources with and without signatures of high mass star formation. In total, 244 sources were observed in both ammonia transitions, using the Parkes radio telescope. Of these, 138 had detections ($>3\text{-}\sigma$) in $\text{NH}_3(1,1)$, including two sources with two velocity components, and 102 in $\text{NH}_3(2,2)$. The MM-only sources are not more or less likely to be detected in either transition than the sources with a methanol maser and/or radio continuum association.

The spectral line properties of the sources have been determined from gaussian fits to the lines: linewidth, flux density, opacity. In addition, physical parameters, such as the rotational and kinetic temperatures as well as the column density, were derived from the spectra. From the kinetic temperature, and revisiting previous SED modelling techniques (Hill et al. 2009), we have determined the mass and luminosity of the sources in the sample. We have used the Bayesian inference method of SED modelling, which provides robust estimates of the parameters as well as good es-

timates of the uncertainties associated with each parameter, further allowing robust statistical conclusions.

Combining continuum and line observations has proven to be quite powerful. In our case, ammonia observations and SED modelling are very complementary in terms of parameter determinations. It is clear, that the kinetic temperature, as derived from ammonia, used in combination with SED modelling has constrained the range of validity for the temperature, which in turn has constrained the range of validity for the mass and luminosity for each of the sources in our sample.

The MM-only sources, those with no overt signs of massive star formation, have smaller $\text{NH}_3(1,1)$ and $(2,2)$ linewidths on average compared with sources associated with a methanol maser and/or radio continuum source. They are also less massive and smaller on average but reach the same upper values for both parameters. Because the MM-only sources have similar brightness/flux, column densities and similar temperatures as star forming sources, they have the potential to form stars. The least massive MM-only sources, cannot form high mass stars and will likely proceed to form intermediate mass stars, whilst the more massive clumps, are more interestingly strong candidates for early stage massive protostars. The different hypotheses will result in different internal structures.

Higher spatial resolution observations with ALMA will allow resolution of the internal structures of the MM-only cores, which may then allow us to distinguish between starless cores that will beget massive stars and those that are transient.

ACKNOWLEDGMENTS

The authors would like to thank S. Mader for observational support and J. Reynolds & E. Carretti for help with calibration of the observations and derivation of the gain elevation correction. We also extend thanks to an anonymous referee whose comments served to improve the manuscript. C. Pinte acknowledges funding support of the European Commissions Seventh Framework Program as a Marie Curie Intra-European Fellow (PIEF-GA-2008-220891). The Parkes telescope is part of the Australia Telescope which is funded by the Commonwealth of Australia for operation as a National Facility managed by CSIRO.

REFERENCES

- André P., Ward-Thompson D., Barsony M., 2000, *Protostars and Planets IV*, p. 59
- Bertoldi F., McKee C. F., 1992, *ApJ*, 395, 140
- Beuther H., Churchwell E. B., McKee C. F., Tan J. C., 2007, in Reipurth B., Jewitt D., Keil K., eds, *Protostars and Planets V The Formation of Massive Stars*. pp 165–180
- Beuther H., Henning T., 2009, *A&A*, 503, 859
- Beuther H., Schilke P., Menten K. M., Motte F., Sridharan T. K., Wyrowski F., 2002, *ApJ*, 566, 945
- Bonnell I. A., Bate M. R., Zinnecker H., 1998, *MNRAS*, 298, 93
- Buckle et al. J. V., 2009, *ArXiv e-prints*
- Chabrier G., 2003, *ApJL*, 586, L133

- Churchwell E., Walmsley C. M., Cesaroni R., 1990, *A&AS*, 83, 119
- Danby G., Flower D. R., Valiron P., Schilke P., Walmsley C. M., 1988, *MNRAS*, 235, 229
- Evans N. J., Shirley Y. L., Mueller K. E., Knez C., 2002, in Crowther P., ed., *Hot Star Workshop III: The Earliest Phases of Massive Star Birth Vol. 267 of Astronomical Society of the Pacific Conference Series, The Formation and Early Evolution of Massive Stars*. pp 17–+
- Garay G., Lizano S., 1999, *PASP*, 111, 1049
- Hill T., Burton M. G., Minier V., Thompson M. A., Walsh A. J., Hunt-Cunningham M., Garay G., 2005, *MNRAS*, 363, 405
- Hill T., Pinte C., Minier V., Burton M. G., Cunningham M. R., 2009, *MNRAS*, 392, 768
- Hill T., Thompson M. A., Burton M. G., Walsh A. J., Minier V., Cunningham M. R., Pierce-Price D., 2006, *MNRAS*, 368, 1223
- Ho P. T. P., Townes C. H., 1983, *Ann. Rev. Astr. Ap.*, 21, 239
- Jackson J. M., Finn S. C., Rathborne J. M., Chambers E. T., Simon R., 2008, *ApJ*, 680, 349
- Jijina J., Myers P. C., Adams F. C., 1999, *Astrophys. J. Supp. Series*, 125, 161
- Krugel E., Walmsley C. M., 1984, *A&A*, 130, 5
- Krumholz M. R., Klein R. I., McKee C. F., Offner S. S. R., Cunningham A. J., 2009, *Science*, 323, 754
- Li D., Goldsmith P. F., Menten K., 2003, *ApJ*, 587, 262
- Longmore S. N., Burton M. G., Barnes P. J., Wong T., Purcell C. R., Ott J., 2007, *MNRAS*, 379, 535
- Longmore S. N., Burton M. G., Keto E., Kurtz S., Walsh A. J., 2009, *MNRAS*, pp 1151–+
- Longmore S. N., Burton M. G., Minier V., Walsh A. J., 2006, *MNRAS*, 369, 1196
- Longmore S. N., Burton M. G., Purcell C. R., Barnes P., Ott J., 2008, in Beuther H., Linz H., Henning T., eds, *Massive Star Formation: Observations Confront Theory Vol. 387 of Astronomical Society of the Pacific Conference Series, Determining the Relative Evolutionary Stages of Very Young Massive Star Formation Regions*. pp 58–64
- McKee C. F., Tan J. C., 2003, *ApJ*, 585, 850
- Menten K. M., Pillai T., Wyrowski F., 2005, in *IAU Symposium Initial conditions for massive star birth-Infrared dark clouds*. pp 23–34
- Minier V., Booth R. S., Conway J. E., 2000, *A&A*, 362, 1093
- Minier V., Burton M. G., Hill T., Pestalozzi M. R., Purcell C. R., Garay G., Walsh A. J., Longmore S., 2005, *A&A*, 429, 945
- Molinari S., Brand J., Cesaroni R., Palla F., 1996, *A&A*, 308, 573
- Pestalozzi M. R., Minier V., Booth R. S., 2005, *A&A*, 432, 737
- Pillai T., Wyrowski F., Carey S. J., Menten K. M., 2006, *A&A*, 450, 569
- Pinte et al. C., 2008, *A&A*, 489, 633
- Robitaille T. P., Whitney B. A., Indebetouw R., Wood K., Denzmore P., 2006, *Astrophys. J. Supp. Series*, 167, 256
- Schnee S., Sargent A., 2007, in *Bulletin of the American Astronomical Society Vol. 38 of Bulletin of the American Astronomical Society, Dust and Gas Temperature of the Prestellar Core TMC-1C*. pp 879–
- Sridharan T. K., Beuther H., Saito M., Wyrowski F., Schilke P., 2005, *ApJL*, 634, L57
- Sridharan T. K., Beuther H., Schilke P., Menten K. M., Wyrowski F., 2002, *ApJ*, 566, 931
- Tafalla M., Myers P. C., Caselli P., Walmsley C. M., 2004, *A&A*, 416, 191
- Ungerechts H., Winnewisser G., Walmsley C. M., 1986, *A&A*, 157, 207
- Walsh A. J., Burton M. G., Hyland A. R., Robinson G., 1998, *MNRAS*, 301, 640
- Whitney B. A., Wood K., Bjorkman J. E., Cohen M., 2003, *ApJ*, 598, 1079
- Williams S. J., Fuller G. A., Sridharan T. K., 2004, *A&A*, 417, 115
- Zinnecker H., Yorke H. W., 2007, *Ann. Rev. Astr. Ap.*, 45, 481

APPENDIX A: NH₃(1,1) AND (2,2) SPECTRA

The NH₃(1,1) and (2,2) inversion spectra detected by the K-band receiver on the Parkes Telescope are presented here for all sources, including those in the sample figure (Fig. 1). Sources are presented in right ascension order, consistent with Table 1 and the complementary continuum images of Hill et al. (2005). The x-axis is in units of velocity (kms⁻¹) whilst the y-axis is the flux density (Jy/beam) or strength of the detection. Both the V_{LSR} and flux density of the sources are presented in Table 1. The fits as returned from CLASS are overlaid on the spectra in green.

This paper has been typeset from a T_EX/L^AT_EX file prepared by the author.